

# Post-collisional, K-rich mafic magmatism in south Tibet: constraints on Indian slab-to-wedge transport processes and plateau uplift

Zhengfu Guo · Marjorie Wilson · Maoliang Zhang ·  
Zhihui Cheng · Lihong Zhang

Received: 11 July 2012 / Accepted: 1 February 2013 / Published online: 13 March 2013  
© Springer-Verlag Berlin Heidelberg 2013

**Abstract** Post-collisional (23–8 Ma), potassium-rich (including ultrapotassic and potassic) mafic magmatic rocks occur within the north–south-trending Xuruco lake–Dangre Yongcuo lake (XDY) rift in the Lhasa terrane of the southern Tibetan Plateau, forming an approximately 130-km-long semi-continuous magmatic belt. They include both extrusive and intrusive facies. Major and trace element and Sr–Nd–Pb isotopic data are presented for all of the known exposures within the XDY rift. The potassium-rich, mafic igneous rocks are characterized by high MgO (5.9–10.8 wt.%), K<sub>2</sub>O (4.81–10.68 wt.%), Ba (1,782–5,618 ppm) and Th (81.3–327.4 ppm) contents, and relatively high SiO<sub>2</sub> (52.76–58.32 wt.%) and Al<sub>2</sub>O<sub>3</sub> (11.10–13.67 wt.%). Initial Sr isotopic compositions are extremely radiogenic (0.712600–0.736157), combined with low (<sup>206</sup>Pb/<sup>204</sup>Pb)<sub>i</sub> (18.28–18.96) and (<sup>143</sup>Nd/<sup>144</sup>Nd)<sub>i</sub> (0.511781–0.512046). Chondrite-normalized rare earth element patterns display relatively weak negative Eu anomalies. Primitive mantle-normalized incompatible trace element patterns exhibit strong enrichments in large ion lithophile elements relative to high-field-strength elements

and display strongly negative Ta–Nb–Ti anomalies. The combined major and trace element and Sr–Nd–Pb isotopic characteristics of the K-rich igneous rocks suggest that the primitive magmas were produced by 1–10 % partial melting of an asthenospheric mantle source enriched by both fluids and partial melts derived from Indian passive continental margin sediments subducted into the shallow mantle as a consequence of the northward underthrusting of the Indian continental lithosphere beneath Tibet since the India–Asia collision at ~55 Ma. The best-fit model results indicate that a melt with trace element characteristics similar to those of the K-rich rocks could be generated by 8–10 % partial melting of a metasomatized mantle source in the south and 1–2 % melting in the north of the XDY rift. Trace element and Sr–Nd–Pb isotopic modeling indicate that the proportion of fluid derived from the subducted sediments, for which we use as a proxy the Higher Himalayan Crystalline Sequence (HHCS), in the mantle source region increases from north (rear-arc) to south (front-arc), ranging from 0 to 5 %, respectively. Correspondingly, the proportion of the melt derived from the subducted HHCS in the source increases from north (2 %) to south (15 %). The increasing proportion of the fluid and melt component in the mantle source from north to south, together with a southward decreasing trend in the age of the K-rich magmatism within the XDY rift, is inferred to reflect rollback of the subducted Indian lithospheric mantle slab during the period 25–8 Ma. Slab rollback may be linked to a decreasing convergence rate between India and Asia. As a consequence of slab rollback at 25 Ma beneath the Lhasa terrane, its geodynamic setting was transformed from a convergent (55–25 Ma) to an extensional (25–8 Ma) regime. The occurrence of K-rich magmatism during the period 25–8 Ma is a consequence of the decompression melting of an enriched mantle source,

Communicated by H. Keppler.

**Electronic supplementary material** The online version of this article (doi:10.1007/s00410-013-0860-y) contains supplementary material, which is available to authorized users.

Z. Guo (✉) · M. Zhang · Z. Cheng · L. Zhang  
Key Laboratory of Cenozoic Geology and Environment, Institute of Geology and Geophysics, Chinese Academy of Sciences, P.O. Box 9825, Beijing 100029, China  
e-mail: zfguo@mail.iggcas.ac.cn

M. Wilson  
School of Earth and Environment, University of Leeds, Leeds LS2 9JT, UK

which may signal the onset of extension in the southern Tibetan Plateau and provide a petrological record of the extension process.

**Keywords** Ultrapotassic and potassic magmatic rocks · Slab rollback · Enriched asthenospheric mantle · Extension · Tibetan Plateau

## Introduction

The geodynamic processes responsible for uplift and extensional tectonics forming N–S-trending rifts in the Tibetan Plateau, postdating the India–Asia collision, have long been a subject of debate (e.g., Yin and Harrison 2000; Blisniuk et al. 2001; Gao et al. 2007; Guo et al. 2007). Understanding the cause of post-collisional, potassium-rich magmatism in the Lhasa terrane of the southern Tibetan Plateau, which is distributed along a series of N–S-trending rifts (Fig. 1), can provide important constraints on the mechanism of plateau uplift and lithospheric extension (e.g., Williams et al. 2001, 2004; Gao et al. 2007). Although there have been a number of studies on these magmatic rocks (e.g., Coulon et al. 1986; Pearce and Mei 1988; Arnaud et al. 1992; Turner et al. 1996; Chung et al. 1998, 2005; Williams et al. 2001, 2004; Ding et al. 2003; Nomade et al. 2004; Mo et al. 2006a, 2007; Gao et al. 2007; Zhao et al. 2009; Chen et al. 2010, 2011), their petrogenesis remains highly controversial. Most of the previous studies have focused on individual volcanic fields, and petrogenetic models have not been fully integrated in a geodynamic context.

Three hypotheses have been suggested to explain the post-collisional, potassium-rich magmatism. In the first, the magmatism was thought to result from convective removal of the lower part of previously thickened lithospheric mantle (e.g., Turner et al. 1993, 1996; Chung et al. 1998, 2005; Williams et al. 2001, 2004; Zhao et al. 2009). In the second, the magmatism was attributed to intracontinental subduction of Indian continental lithosphere (e.g., Pearce and Mei 1988; Arnaud et al. 1992; Tapponnier et al. 2001; Ding et al. 2003). In the third, the magmatism was linked to break-off of a northward subducted slab of Indian continental lithosphere (e.g., Miller et al. 1999; DeCelles et al. 2002; Kohn and Parkinson 2002; Maheo et al. 2002). The lack of detailed field sampling and of comprehensive petrological and geochemical data has precluded further constraints on the petrogenesis of these post-collisional magmas.

To further understand the relationship between the occurrence of the north–south-trending rifts and the petrogenesis of the post-collisional, K-rich magmas, this study focuses on a N–S-trending, 130-km-long, K-rich magmatic belt perpendicular to the Indus–Tsangpo suture (ITS) within the Lhasa terrane in south Tibet (Fig. 1). This includes five volcanic

fields from north (rear-arc) to south (front-arc), all of which are located within the N–S-trending Xuruco lake–Dangre Yongcuo lake rift system (hereafter XDY rift), bounded by normal faults (Fig. 1b). The XDY rift is the longest, N–S-trending graben in south Tibet (Kapp et al. 2007; Royden et al. 2008) and has the highest proportion of mafic lava flows.

Recent seismic tomographic studies (e.g., Li et al. 2008; He et al. 2010; Zhao et al. 2011) have indicated the presence of a slab of subducted Indian continental lithosphere beneath southern Tibet. In this study we explore the role of metasomatic components (fluids and melts) released from this subducted Indian continental lithosphere into the overlying asthenospheric mantle wedge in the petrogenesis of the K-rich magmas. Additionally, we further explore the link between slab-to-wedge fluid/melt transfer processes and plateau uplift in south Tibet. Our study focuses on the post-collisional, mafic K-rich magmatic rocks within the XDY rift. We have selectively focused only on igneous rocks with high MgO contents to minimize the potential effects of shallow-level crustal contamination and magmatic differentiation.

We report new geochemical data for the most primitive XDY rift K-rich magmatic rocks; these data extend and are complementary to those of previous studies that predominantly focused on the petrogenesis of individual volcanic fields within the rift (e.g., Ding et al. 2003, 2006; Chen et al. 2007; Gao et al. 2007). On the basis of our data and previously published geochemical and geophysical data, we develop a more robust petrogenetic model to better understand the relationship between subducted slab-to-wedge melt/fluid transfer processes and the post-collisional uplift of the Tibetan Plateau.

## Geological setting

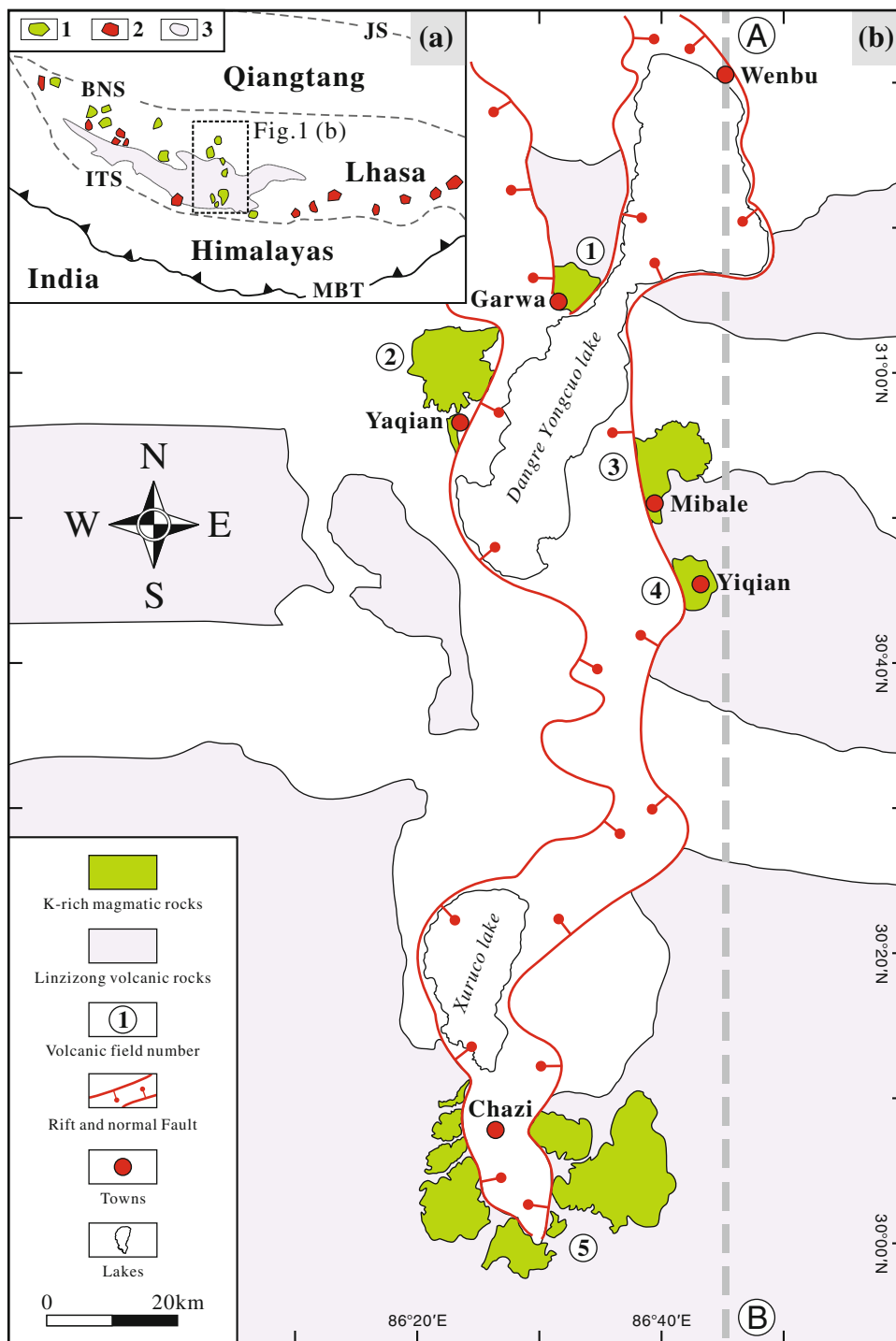
The Tibetan Plateau is a collage of four nearly east–west-trending allochthonous continental terranes which were successively accreted to the southern margin of the Asian continent, mainly in Paleozoic and Mesozoic times (Fig. 1a). From north to south, these are the Kunlun–Qaidam terrane, Songpan–Ganzi terrane, Qiangtang terrane and Lhasa terrane (Fig. 1a). The Lhasa terrane is bounded by the Bangong–Nujiang suture (BNS) to the north and by the Indus–Tsangpo suture (ITS) to the south. This terrane separated from Gondwana in Triassic times and collided with the Qiangtang terrane to the north in Late Jurassic–Early Cretaceous times (Kapp et al. 2003, 2007), forming the BNS. Collision of the Himalayas to the south with the Tibetan Plateau to the north formed the ITS, which marks the boundary between the Indian and Asian continents (e.g., Pearce and Mei 1988; Tapponnier et al. 2001; Mo et al. 2003; Deng et al. 2004). Most studies support the traditional view of India–Asia collision at 55–50 Ma (e.g., Patriat and Achache 1984; Klootwijk et al. 1992; Leech

et al. 2005; Tapponnier et al. 2001; Zhu et al. 2005; Royden et al. 2008; Najman et al. 2010; Sun et al. 2012), although this remains controversial (e.g., Ding et al. 2003, 2005; Mo et al. 2003, 2008; Ali and Aitchison 2008; Chen et al. 2010; Cai et al. 2011; Yi et al. 2011).

The Precambrian basement of the Lhasa terrane is comprised of orthogneiss with an age of 852 Ma (Guynn et al. 2006). Its Phanerozoic cover sequences mainly

comprise Paleozoic to Mesozoic sedimentary rocks and interbedded Jurassic–Cretaceous volcanic rocks (Zhu et al. 2008). Magmatic activity became important during the Cenozoic in south Tibet. The Cenozoic magmatic rocks in the Lhasa terrane are subdivided into three groups based on their age relationships and geochemical characteristics. Group 1 comprises the Linzizong volcanic rocks and Transhimalaya (or Gangdese) batholiths (Fig. 1a), which

**Fig. 1** **a** Overview map showing the distribution of Cenozoic magmatic rocks in southern Tibet (modified from DeCelles et al. 2002; Guo et al. 2007; Liu et al. 2011). 1 Post-collisional, K-rich magmatic rocks, 2 adakites, 3 Linzizong volcanic rocks. The rectangle shows the location of the study area. The dashed lines show the main tectonic sutures. JS Jinsha suture, BNS Bangong–Nujiang suture, ITS Indus–Tsangpo suture, MBT Main Boundary Thrust. **b** Map showing the distribution of post-collisional, K-rich magmatic rocks in the XDY rift (modified from Liao et al. 2002; Ding et al. 2003; Chen et al. 2007; Gao et al. 2007). The numbers in circles represent the individual volcanic fields as follows: 1 Garwa, 2 Yaqian, 3 Mibale, 4 Yiqian, 5 Chazi



range in age from ~65 to 40 Ma (Scharer 1984; Coulon et al. 1986; Zhou et al. 2004; Mo et al. 2005, 2006a, b; Wen et al. 2008). Mo et al. (2008) have suggested that the Linzizong parental magmas resulted from melting of a subducted Neotethyan ocean lithospheric slab beneath south Tibet, although the volcanism has traditionally been attributed to northward subduction of Neotethyan oceanic lithosphere beneath the Lhasa terrane (e.g., Coulon et al. 1986). These subduction-related calc-alkaline igneous rocks are extensively distributed in the southern part of the Lhasa terrane (Fig. 1), forming an Andean-type active continental margin. Group 2 magmatic rocks are Miocene (18–12 Ma) adakites; they are mainly restricted to the eastern part of the Lhasa terrane (Fig. 1a). Their petrogenesis has been widely attributed to melting of thickened mafic lower crust (Chung et al. 2003; Hou et al. 2004; Guo et al. 2007) or subducted oceanic crust (Qu et al. 2004). Group 3 magmatic rocks comprise the post-collisional ultrapotassic and potassic rock types which are the focus of this study (Fig. 1); their ages range from 25 to 8 Ma based on  $^{40}\text{Ar}/^{39}\text{Ar}$ , K–Ar, Rb–Sr and single-crystal zircon U–Pb dating (e.g., Coulon et al. 1986; Yin et al. 1994; Miller et al. 1999; Williams et al. 2001, 2004; Ding et al. 2003; Nomade et al. 2004; Mo et al. 2006a; Zhao et al. 2006, 2009; Sun et al. 2008; Chen et al. 2010). These K-rich igneous rocks include both extrusive and intrusive facies. The intrusive facies (dikes and plugs) crosscut the Gangdese granite batholiths, the Linzizong volcanic succession and the underlying sedimentary formations, whereas the extrusive facies unconformably overlie the magmatic rocks of Group 1 and the underlying Paleozoic–Mesozoic sedimentary rocks.

Previous studies (e.g., Williams et al. 2001, 2004; Ding et al. 2003; Chung et al. 2005; Mo et al. 2006b; Gao et al. 2007; Zhao et al. 2009; Chen et al. 2010, 2012) have demonstrated that the Group 3 magmatic rocks have spatial distributions and geochemical characteristics which are clearly different from those of Group 1 and Group 2. They occur as small-volume lava flows, plugs and dike swarms within a series of north–south-trending rifts bounded by normal faults, including the XDY rift (Fig. 1b). Seismic tomographic studies (e.g., Li et al. 2008) indicate that the northward subducted Indian continental lithosphere slab lies at a depth of ~125 km beneath the southernmost Chazi volcanic field and at ~200 km depth beneath the northernmost Garwa volcanic field (Fig. 1b).

Five volcanic fields are located within the XDY rift, which form the basis of this study (Fig. 1). They include lava flows, plugs and dykes, forming an N–S-trending, 130-km-long, magmatic belt extending from the Garwa volcanic field in the north, through the Yaqian, Mibale and Yiqian volcanic fields to the Chazi volcanic field in the south (Fig. 1b). Exposures range from less than 10 to

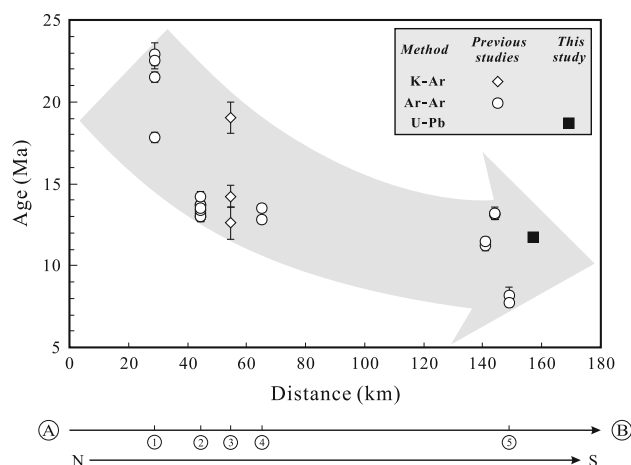


**Fig. 2** Decreasing trend in the ages of the post-collisional, K-rich magmatic rocks from north to south in the XDY rift. The location of the cross section is shown by the dashed gray line A–B in Fig. 1. The numbers within the circles along the profile represent the numbers of the volcanic fields as shown in Fig. 1. The x-coordinate is the distance (in km) of the volcanic fields from Wenbu in Fig. 1. The ages of the magmatic rocks are from Table 1

~300 km<sup>2</sup>. The ages of the magmatic rocks decrease from north (rear-arc) to south (front-arc) along the rift (Fig. 2; Table 1).

## Petrography

All the analyzed samples are unweathered and show no evidence of significant hydrothermal alteration. They have porphyritic textures with phenocrysts of 1–5 mm in size. Their petrographic characteristics are summarized in Table 2. The phenocryst minerals consist of clinopyroxene, phlogopite, and rare olivine, sanidine and apatite. The groundmass includes phlogopite, clinopyroxene, sanidine, apatite, Fe–Ti oxides, leucite, zircon and glass (Table 2), similar to the typical mineralogical assemblage of orogenic lamproites from central Italy (Conticelli and Peccerillo 1992; Conticelli et al. 2009), SE Spain (Venturelli et al. 1984; Benito et al. 1999; Conticelli et al. 2009) and the East European Alpine belt (Altherr et al. 2004).

## Analytical methods

### Single-zircon U–Pb geochronology

Single-zircon U–Pb dating was conducted using the SHRIMP II at the Institute of Geology, Chinese Academy of Geological Sciences (Beijing, China). Zircon grains were separated under a binocular microscope from samples of ~10 kg in weight, cast along with zircon U–Pb international standards (TEM and SL13) in an epoxy mount and

**Table 1** Ages of the post-collisional, K-rich magmatic rocks in the XDY rift of south Tibet

Field no.	Sample no.	Field name	Dating method	Mineral and whole rock dated	Age (Ma)	Data sources
1	99T60	Garwa	$^{40}\text{Ar}/^{39}\text{Ar}$	Sanidine	$22.9 \pm 0.7$ (a)	Ding et al. (2003)
1	99T60	Garwa	$^{40}\text{Ar}/^{39}\text{Ar}$	Sanidine	$21.5 \pm 0.3$ (b)	Ding et al. (2003)
1	99T62	Garwa	$^{40}\text{Ar}/^{39}\text{Ar}$	Sanidine	$22.5 \pm 0.5$ (a)	Ding et al. (2003)
1	99T62	Garwa	$^{40}\text{Ar}/^{39}\text{Ar}$	Sanidine	$17.8 \pm 0.3$ (b)	Ding et al. (2003)
2	DR01-01	Yaqian	$^{40}\text{Ar}/^{39}\text{Ar}$	Biotite	$13.2 \pm 0.3$ (c)	Zhao et al. (2006)
2	DR01-02	Yaqian	$^{40}\text{Ar}/^{39}\text{Ar}$	Sanidine	$13.0 \pm 0.3$ (c)	Zhao et al. (2006)
2	DR03	Yaqian	$^{40}\text{Ar}/^{39}\text{Ar}$	Sanidine	$13.7 \pm 0.3$ (c)	Zhao et al. (2006)
2	DR04	Yaqian	$^{40}\text{Ar}/^{39}\text{Ar}$	Sanidine	$13.0 \pm 0.3$ (c)	Zhao et al. (2006)
2	DR01-1	Yaqian	$^{40}\text{Ar}/^{39}\text{Ar}$	Biotite	$13.4 \pm 0.2$ (a)	Zhao et al. (2009)
2	DR01-2	Yaqian	$^{40}\text{Ar}/^{39}\text{Ar}$	Sanidine	$13.7 \pm 0.2$ (a)	Zhao et al. (2009)
2	DR03	Yaqian	$^{40}\text{Ar}/^{39}\text{Ar}$	Sanidine	$14.2 \pm 0.3$ (a)	Zhao et al. (2009)
2	DR04	Yaqian	$^{40}\text{Ar}/^{39}\text{Ar}$	Sanidine	$13.5 \pm 0.2$ (a)	Zhao et al. (2009)
3	8030-5	Mibale	K–Ar	Whole rock	$19.04 \pm 0.97$	Gao et al. (2007); Xie et al. (2004)
3	8030-5	Mibale	K–Ar	Whole rock	$12.60 \pm 0.97$	Liao et al. (2002), Xie et al. (2004)
3	8030-18	Mibale	K–Ar	Whole rock	$14.22 \pm 0.68$	Xie et al. (2004)
4	2003T536	Yiqian	$^{40}\text{Ar}/^{39}\text{Ar}$	Biotite	$13.5 \pm 0.1$ (a)	Ding et al. (2006)
4	2003T536	Yiqian	$^{40}\text{Ar}/^{39}\text{Ar}$	Biotite	$12.8 \pm 0.1$ (c)	Ding et al. (2006)
5	XR01-03	Chazi	$^{40}\text{Ar}/^{39}\text{Ar}$	Biotite	$11.2 \pm 0.3$ (c)	Zhao et al. (2006)
5	XR01-3	Chazi	$^{40}\text{Ar}/^{39}\text{Ar}$	Biotite	$11.5 \pm 0.2$ (a)	Zhao et al. (2009)
5	G8	Chazi	U–Pb	Zircon	$11.70 \pm 0.15$	This study
5	99T154	Chazi	$^{40}\text{Ar}/^{39}\text{Ar}$	Sanidine	$13.1 \pm 0.3$ (a)	Ding et al. (2003)
5	99T154	Chazi	$^{40}\text{Ar}/^{39}\text{Ar}$	Sanidine	$13.2 \pm 0.4$ (b)	Ding et al. (2003)
5	99T145	Chazi	$^{40}\text{Ar}/^{39}\text{Ar}$	Sanidine	$8.2 \pm 0.5$ (a)	Ding et al. (2003)
5	99T145	Chazi	$^{40}\text{Ar}/^{39}\text{Ar}$	Sanidine	$7.7 \pm 0.2$ (b)	Ding et al. (2003)

Field no. refers to number of the volcanic field in Fig. 1. Field name corresponds to that in Fig. 1. Age categories of the post-collisional, K-rich magmatic rocks, which are shown by letters in parentheses, are as follows: (a) plateau age; (b) total gas age; (c) isochron age

then polished to section the crystals for analysis. Zircons were documented using both transmitted and reflected light photomicrographs and backscattered electron images, and the mount was vacuum coated with a 500-nm layer of high-purity gold (Au). A cathodoluminescence (CL) investigation was conducted at the Microprobe Laboratory of the Institute of Geology and Geophysics, Chinese Academy of Science. U–Th–Pb isotopic ratios were corrected for instrumental interelement fractionation using the zircon standard TEM with  $^{206}\text{Pb}/^{238}\text{U} = 0.0668$  at 417 Ma. U, Th and Pb absolute abundances were calibrated using the zircon standard SL13 (572 Ma) with U = 238 ppm and Th = 18 ppm (Black et al. 2003a, b, 2004). The two zircon standards were provided by the Australian National University. Data were handled using the Ludwig SQUID 1.0 and ISOPLOT programs. Measured compositions were corrected for common Pb using non-radiogenic  $^{204}\text{Pb}$ . Detailed analytical procedures for instrument operation and data calculation, following those established in RSES, Australian National University, are summarized elsewhere (e.g., Chung et al. 2003; Hou et al. 2004; Qu et al. 2009). Analysis conditions are a ca 15 nA, 10 kV  $\text{O}^{2-}$  beam with

a spot size of 25–30  $\mu\text{m}$  in diameter. A single spot on each zircon grain was analyzed for about 20 min; one sample required analysis of 8–15 spots on different zircon grains for the age calculation. A zircon U–Pb international standard was analyzed for every three U–Pb single-spot analyses of the samples in order to monitor the analytical accuracy, external precision and instrumental drift. Thus, a single sample was continuously analyzed for about 5–8 h. The mass resolution used for measuring Pb/Pb and Pb/U isotopic ratios was about 5,000. The U–Pb data are presented as a concordia plot (Fig. 3) and in Table 3. The uncertainties of the individual analyses are shown at the  $1\sigma$  level (Table 3). Magmatic crystallization ages, indicated by the mean  $^{206}\text{Pb}/^{238}\text{U}$  age, are reported with a 95 % confidence interval ( $2\sigma$ ).

#### Whole-rock major and trace element analyses

Samples 4–5 kg in weight were cut into several thin slices. Fresh slices were cleaned three times using deionized water, dried and then crushed in an agate mortar for whole-rock major element, trace element and Sr–Nd–Pb isotopic analysis.

**Table 2** Phenocryst and groundmass mineral assemblages of the XDY magmatic rocks

Field no.	Sample no.	Field name	Mg-no.	Rock type	Phenocrysts	Groundmass
1	DY-7	Garwa	0.75	S3	Phl + Cpx + Ol + Lc	Phl + Cpx + Sani + Ap + Fe-Ti + G
1	DC2	Garwa	0.71	U3	Phl + Cpx + Ap + Sani	Phl + Cpx + Lc + Ol + Ap + Fe-Ti + Zr
1	D509	Garwa	0.75	U3	Phl + Cpx + Ol + Lc	Phl + Cpx + Lc + Ap + Fe-Ti + G
1	DG43	Garwa	0.74	S3	Phl + Cpx + Lc + Ol	Phl + Cpx + Sani + Ap + Fe-Ti
2	YE51	Yaqian	0.76	S3	Cpx + Phl + Ap	Sani + Phl + Cpx + Ol + Ap + Fe-Ti
2	YC08	Yaqian	0.73	S3	Lc + Cpx + Phl + Ap + Ol	Sani + Phl + Cpx + Ap + Fe-Ti + G
2	YG13	Yaqian	0.78	S3	Phl + Cpx + Ol	Lc + Phl + Cpx + Ap + Fe-Ti
2	YF12	Yaqian	0.76	S3	Cpx + Phl + Ol	Sani + Phl + Cpx + Ap + Zr
2	YA32	Yaqian	0.69	S3	Lc + Cpx + Phl + Ol	Sani + Phl + Cpx + Tit + Fe-Ti + G
3	MH78	Mibale	0.77	S3	Ol + Cpx + Phl	Sani + Phl + Cpx + Ap + Fe-Ti + G
3	MH69	Mibale	0.81	S3	Ol + Cpx + Phl	Lc + Phl + Cpx + Fe-Ti
3	MG-3	Mibale	0.74	S3	Phl + Cpx + Sani	Sani + Phl + Cpx + Ap + Fe-Ti + Tit
3	MY1	Mibale	0.73	U3	Lc + Cpx + Phl	Cpx + Phl + Ap + Fe-Ti + G
3	MK09	Mibale	0.75	S3	Lc + Cpx	Phl + Cpx + Fe-Ti + Zr
3	MR21	Mibale	0.76	S3	Ol + Cpx + Phl	Cpx + Phl + Lc + Fe-Ti + G
3	MA75	Mibale	0.76	S3	Ol + Cpx + Phl	Sani + Cpx + Phl + Ap + Fe-Ti + G
3	MX5	Mibale	0.77	S3	Phl + Cpx	Sani + Phl + Cpx + Fe-Ti
5	G8	Chazi	0.70	S3	Phl + Cpx	Lc + Ap + Cpx + Zr + Fe-Ti + G
5	C10	Chazi	0.70	S3	Phl + Cpx	Lc + Ap + Cpx + Fe-Ti + G
5	CV5	Chazi	0.69	S3	Phl + Cpx	Sani + Ap + Cpx + Fe-Ti + G
5	C76	Chazi	0.70	S3	Phl + Cpx	Lc + Cpx + Ol + Phl + Fe-Ti + G
5	CH4	Chazi	0.69	S3	Phl + Cpx + Lc	Sani + Ap + Cpx + Fe-Ti
5	CH7	Chazi	0.78	S2	Phl + Cpx + Ol	Lc + Ap + Cpx + Phl + Fe-Ti
5	C03	Chazi	0.80	S2	Phl + Cpx + Ol	Lc + Cpx + Phl + Fe-Ti + G
5	CX38	Chazi	0.70	S3	Lc + Cpx + Phl	Lc + Phl + Cpx + Fe-Ti
5	C25	Chazi	0.75	S3	Phl + Cpx + Lc	Sani + Cpx + Ap + Fe-Ti + G

Field no. refers to number of the volcanic field in Fig. 1. Field name corresponds to that in Fig. 1

Ap Apatite, Cpx clinopyroxene, Fe-Ti Fe-Ti oxides, G glass, Lc leucite, Ol olivine, Phl phlogopite, Sani sanidine, Tit titanite, Zr zircon  
S2 basaltic trachyandesite, S3 trachyandesite, U3 tephriphonolite

Whole-rock major element contents (wt.%) were determined on fused glass disks by X-ray fluorescence (XRF) using an XRF-1500 sequential spectrometer (SHIMADZU, Japan) at the Institute of Geology and Geophysics, Chinese Academy of Sciences, Beijing (IGGCAS). Sample powders (0.6 g) were fused with  $\text{Li}_2\text{B}_4\text{O}_7$  (6 g) in a TR-1000S automatic bead fusion furnace (SHIMADZU, Japan) at 1,100 °C for 10 min. Loss on ignition (LOI) was determined by ignition at 1,100 °C for 10 h of 2 g whole-rock powder. The analytical precision was better than 2 % relative. The detailed operating procedure follows that reported by Guo et al. (2006). Analytical data are presented in electronic supplementary material 1.

Rare earth element (REE) and trace element contents were analyzed by inductively coupled plasma mass spectrometry (ICP-MS) at IGGCAS using a FINNIGAN MAT II element system. Whole-rock powders (40 mg) were weighed and dissolved in 1 ml distilled 20 N HF and

0.5 ml 7.5 N  $\text{HNO}_3$  ( $\text{HNO}_3/\text{H}_2\text{O} = 1:1$ , volume ratio) in 7-ml Savillex Teflon screw-cap capsules and then were ultrasonically stirred for 15 min. Subsequently, the solutions were evaporated at 150 °C to dryness, and the residue was digested with 1.5 ml HF and 0.5 ml  $\text{HNO}_3$  ( $\text{HNO}_3/\text{H}_2\text{O} = 1:1$ ) in Teflon screw-cap capsules. The solutions were first heated at 130 °C for 2 h, and then the temperature was gradually increased up to 170 °C over 24 h. The solutions were then maintained at 170 °C for 10 days, dried and redissolved in 2 ml  $\text{HNO}_3$  ( $\text{HNO}_3/\text{H}_2\text{O} = 1:1$ ) in the capsules. The solutions were heated at 150 °C for 5 h and then evaporated, dried and redissolved in 2 ml  $\text{HNO}_3$  ( $\text{HNO}_3/\text{H}_2\text{O} = 1:1$ ) and 2 ml 1 %  $\text{HNO}_3$  at 150 °C for 5 h in screw-cap capsules in order to ensure that the samples were completely dissolved. The solutions were put into plastic beakers, and then 1 ml 500 ppb In was added as an internal standard. Finally, the solutions were diluted in 1 %  $\text{HNO}_3$  to 50 ml for analysis by ICP-MS. A blank solution

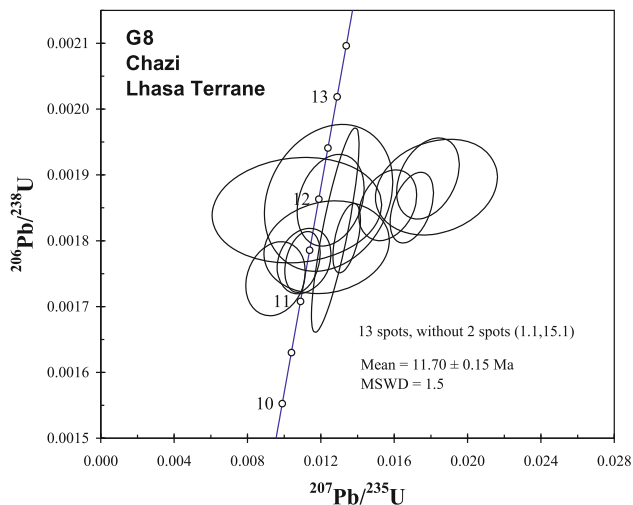


**Fig. 3** Zircon U–Pb concordia diagram for the K-rich volcanic rock (G8) from Chazi. Data are from Table 3

was prepared; the total procedural blanks were <50 ng for all the trace elements reported in electronic supplementary material 1. During the analytical runs, frequent standard calibrations were performed to correct for instrumental signal drift following the procedure of Guo et al. (2006). Four replicates and two international standards (BHVO-1 and AGV-1) were prepared using the same procedure to monitor the analytical reproducibility. The discrepancy, based on repeated analyses of samples and international standards, is less than 4 % for all the trace elements given in electronic supplementary material 1. Analyses of

the international standards are in excellent agreement with the recommended values (Govindaraju 1994) and deviate less than 5 % from the published values (electronic supplementary material 1). The detailed analytical procedures follow those of Guo et al. (2005, 2006).

#### Sr–Nd–Pb isotopic analyses

Sr–Nd–Pb isotopic analyses were performed on a Finnigan MAT262 mass spectrometer at IGGCAS. For Rb–Sr and Sm–Nd isotopic analyses, whole-rock chips of less than 20 mesh size were used. Before being ground to 200 mesh size (75  $\mu\text{m}$ ) in an agate mortar, the chips were leached in 0.06 N HCl for 1 h at room temperature to minimize the influence of surface alteration or weathering, especially for Sr isotopic ratios. Whole-rock powders (60 mg) were spiked with mixed isotopic tracers ( $^{87}\text{Rb}$ – $^{84}\text{Sr}$  for Rb–Sr isotopic analyses and  $^{149}\text{Sm}$ – $^{150}\text{Nd}$  for Sm–Nd isotopic analyses) and then dissolved with a mixed acid ( $\text{HF}/\text{HClO}_4 = 3:1$ ) in Teflon capsules for 7 days at room temperature. Rb and Sr and rare earth element fractions were separated in solution using AG50 W  $\times$  8 ( $\text{H}^+$ ) cationic ion-exchange resin columns. Sm and Nd were separated from the other rare earth element fractions in solution using AG50 W  $\times$  8 ( $\text{H}^+$ ) cationic ion-exchange columns and P507 extraction and eluviation resin. The collected Sr and Nd fractions were evaporated and dissolved in 2 %  $\text{HNO}_3$  to give solutions for analysis by mass spectrometry. The mass fractionation corrections for Sr and Nd isotopic ratios were based on  $^{86}\text{Sr}/^{88}\text{Sr} = 0.1194$  and  $^{146}\text{Nd}/^{144}\text{Nd} = 0.7219$ , respectively. The international

**Table 3** SHRIMP U–Pb dating of zircon from post-collisional, K-rich magmatic rock G8 from the Chazi volcanic field

Sample no.	U (ppm)	Th (ppm)	$^{232}\text{Th}/^{238}\text{U}$	$^{206}\text{Pb}^*$ (ppm)	$^{207}\text{Pb}^*/^{235}\text{U}$	$\pm\%$ (1 $\sigma$ )	$^{206}\text{Pb}^*/^{238}\text{U}$	$\pm\%$ (1 $\sigma$ )	$^{206}\text{Pb}/^{238}\text{U}$ age (Ma $\pm$ 1 $\sigma$ )
G8-1.1	2,337	993	0.44	3.48	0.01101	5.9	0.001719	2.0	11.07 $\pm$ 0.22
G8-2.1	3,654	9,648	2.73	5.66	0.01341	3.7	0.001804	1.9	11.62 $\pm$ 0.22
G8-3.1	3,015	1,377	0.47	4.70	0.01279	6.7	0.00182	5.7	11.70 $\pm$ 0.66
G8-4.1	837	2,095	2.59	1.31	0.0123	18	0.00179	2.6	11.53 $\pm$ 0.30
G8-5.1	2,925	3,235	1.14	4.47	0.01109	8.7	0.001769	1.9	11.39 $\pm$ 0.21
G8-6.1	905	2,570	2.93	1.47	0.0124	19	0.001865	3.9	12.01 $\pm$ 0.47
G8-7.1	774	2,064	2.76	1.25	0.0107	29	0.001847	2.9	11.89 $\pm$ 0.34
G8-8.1	2,759	1,902	0.71	4.40	0.01696	4.6	0.00185	1.9	11.92 $\pm$ 0.23
G8-9.1	921	2,627	2.95	1.47	0.0125	9.6	0.001862	2.5	11.99 $\pm$ 0.30
G8-10.1	806	1,980	2.54	1.30	0.0183	12	0.001882	2.5	12.12 $\pm$ 0.31
G8-11.1	1,090	2,942	2.79	1.77	0.0178	6.3	0.001895	2.1	12.20 $\pm$ 0.26
G8-12.1	1,830	5,572	3.15	2.91	0.0156	6.7	0.001854	1.9	11.94 $\pm$ 0.23
G8-13.1	6,113	2,384	0.40	9.37	0.01101	5.8	0.001768	1.7	11.39 $\pm$ 0.20
G8-14.1	1,697	3,509	2.14	2.57	0.0095	11	0.001742	2.1	11.22 $\pm$ 0.24
G8-15.1	1,153	2,208	1.98	1.73	0.0113	9.8	0.001727	2.3	11.12 $\pm$ 0.26
Weighted mean of 13 spots (2 $\sigma$ )									11.70 $\pm$ 0.15

Pb\* the radiogenic portions

standard NBS987 gave  $^{87}\text{Sr}/^{86}\text{Sr} = 0.710254 \pm 16$  ( $n = 8$ , 2 sigma) (the recommended value is 0.710240), and international standard NBS607 gave  $^{87}\text{Sr}/^{86}\text{Sr} = 1.20032 \pm 30$  ( $n = 12$ ) (the recommended value is 1.20039). The international La Jolla standard yielded  $^{143}\text{Nd}/^{144}\text{Nd} = 0.511862 \pm 7$  ( $n = 12$ ) (the recommended value is 0.511859), and the international standard BCR-1 yielded  $^{143}\text{Nd}/^{144}\text{Nd} = 0.512626 \pm 9$  ( $n = 12$ ) (the recommended value is 0.512638). The whole procedure blank is less than 200 pg for Rb–Sr isotopic analysis and 50 pg for Sm–Nd isotopic analysis. Analytical errors for Sr and Nd isotopic ratios are given as 2 sigma ( $2\sigma$ ) in Table 4. The  $^{87}\text{Rb}/^{86}\text{Sr}$

and  $^{147}\text{Sm}/^{144}\text{Nd}$  ratios of the samples were calculated using the Rb, Sr, Sm and Nd concentrations obtained by ICP-MS. The initial  $^{87}\text{Sr}/^{86}\text{Sr}$  and  $^{143}\text{Nd}/^{144}\text{Nd}$  ratios were calculated using average ages of the samples based on  $^{40}\text{Ar}/^{39}\text{Ar}$ , K–Ar and U–Pb zircon dating methods (Table 1).

For whole-rock Pb isotopic measurements, in order to minimize contamination from the atmosphere during the crushing process, 100 mesh powders of samples were used. One hundred and fifty milligram of whole-rock powder was weighed and dissolved in Teflon capsules using concentrated HF at 120 °C for 7 days. Pb was separated from the silicate matrix and purified using AG1  $\times$  8 anionic ion-

**Table 4** Sr–Nd isotopic compositions of the XDY K-rich magmatic rocks in south Tibet

Field no.	Sample no.	Field name	$^{87}\text{Sr}/^{86}\text{Sr} \pm 2\sigma$	$^{143}\text{Nd}/^{144}\text{Nd} \pm 2\sigma$	$(^{87}\text{Sr}/^{86}\text{Sr})_i$	$(^{143}\text{Nd}/^{144}\text{Nd})_i$	$\varepsilon\text{Sr}(i)$	$\varepsilon\text{Nd}(i)$
1	DY-7	Garwa	0.712847 $\pm$ 11	0.512056 $\pm$ 7	0.712595	0.512046	115	–11.0
1	DC2	Garwa	0.718046 $\pm$ 14	0.511965 $\pm$ 9	0.717602	0.511954	186	–12.8
1	D509	Garwa	0.716054 $\pm$ 10	0.512026 $\pm$ 7	0.715708	0.512015	159	–11.6
1	DG43	Garwa	0.714758 $\pm$ 9	0.511941 $\pm$ 7	0.714572	0.511929	143	–13.3
2	YE51	Yaqian	0.718364 $\pm$ 13	0.511913 $\pm$ 8	0.718179	0.511906	194	–13.9
2	YC08	Yaqian	0.718469 $\pm$ 12	0.511917 $\pm$ 6	0.718318	0.511909	196	–13.9
2	YG13	Yaqian	0.717351 $\pm$ 11	0.511936 $\pm$ 11	0.717192	0.511929	180	–13.5
2	YF12	Yaqian	0.719673 $\pm$ 14	0.511983 $\pm$ 8	0.719431	0.511976	212	–12.6
2	YA32	Yaqian	0.719041 $\pm$ 13	0.511964 $\pm$ 8	0.718886	0.511956	204	–13.0
3	MH78	Mibale	0.719877 $\pm$ 13	0.511926 $\pm$ 7	0.719678	0.511917	216	–13.7
3	MH69	Mibale	0.721486 $\pm$ 10	0.511992 $\pm$ 6	0.720922	0.511982	233	–12.4
3	MG-3	Mibale	0.719649 $\pm$ 11	0.511961 $\pm$ 8	0.719204	0.511952	209	–13.0
3	MY1	Mibale	0.722672 $\pm$ 12	0.511934 $\pm$ 7	0.722245	0.511925	252	–13.5
3	MK09	Mibale	0.720948 $\pm$ 10	0.511926 $\pm$ 10	0.720700	0.511915	230	–13.7
3	MR21	Mibale	0.725133 $\pm$ 10	0.511854 $\pm$ 6	0.724901	0.511845	290	–15.1
3	MA75	Mibale	0.720861 $\pm$ 12	0.511847 $\pm$ 12	0.720210	0.511839	223	–15.2
3	MX5	Mibale	0.718768 $\pm$ 13	0.511928 $\pm$ 8	0.718285	0.511918	196	–13.7
4	2003T534	Yiqian	0.719910 $\pm$ 10	0.511844 $\pm$ 1	0.719569	0.511835	214	–15.3
4	2003T536	Yiqian	0.720660 $\pm$ 10	0.511822 $\pm$ 1	0.719778	0.511814	217	–15.8
4	2003T539	Yiqian	0.720930 $\pm$ 10	0.511815 $\pm$ 1	0.719802	0.511807	217	–15.9
5	G8	Chazi	0.729418 $\pm$ 10	0.511856 $\pm$ 10	0.728905	0.511846	347	–15.2
5	C10	Chazi	0.735896 $\pm$ 12	0.511874 $\pm$ 9	0.735415	0.511864	439	–14.8
5	CV5	Chazi	0.733316 $\pm$ 16	0.511852 $\pm$ 13	0.732824	0.511844	402	–15.2
5	C76	Chazi	0.730484 $\pm$ 11	0.511793 $\pm$ 7	0.729715	0.511783	358	–16.4
5	CH4	Chazi	0.733043 $\pm$ 12	0.511924 $\pm$ 6	0.732453	0.511916	397	–13.8
5	CH7	Chazi	0.726819 $\pm$ 12	0.511828 $\pm$ 9	0.726344	0.511819	310	–15.7
5	C03	Chazi	0.723169 $\pm$ 15	0.511894 $\pm$ 8	0.722490	0.511885	256	–14.4
5	CX38	Chazi	0.721648 $\pm$ 13	0.511887 $\pm$ 10	0.721363	0.511879	240	–14.5
5	C25	Chazi	0.736552 $\pm$ 11	0.511826 $\pm$ 9	0.736220	0.511817	450	–15.7

Field number refers to number of the volcanic field in Fig. 1

Chondritic uniform reservoir (CHUR) at the present day [ $(^{87}\text{Rb}/^{86}\text{Sr})_{\text{CHUR}} = 0.0847$  (McCulloch and Black 1984);  $(^{87}\text{Sr}/^{86}\text{Sr})_{\text{CHUR}} = 0.7045$  (DePaolo 1988);  $(^{147}\text{Sm}/^{144}\text{Nd})_{\text{CHUR}} = 0.1967$  (Jacobsen and Wasserburg 1980);  $(^{143}\text{Nd}/^{144}\text{Nd})_{\text{CHUR}} = 0.512638$  (Goldstein et al. 1984)] was used for the calculations of the initial epsilon Sr–Nd values.  $\lambda_{\text{Rb}} = 1.42 \times 10^{-11} \text{ year}^{-1}$  (Steiger and Jager 1977);  $\lambda_{\text{Sm}} = 6.54 \times 10^{-12} \text{ year}^{-1}$  (Lugmair and Marti 1978)

Both  $\varepsilon\text{Nd}(i)$  and  $\varepsilon\text{Sr}(i)$  were calculated using the average ages of the volcanic fields (Table 1)

Data for samples (2003T534, 2003T536, 2003T539) from the Yiqian volcanic field are from Ding et al. (2006)

**Table 5** Pb isotopic compositions of the XDY K-rich magmatic rocks in south Tibet

Field no.	Sample no.	Field name	$^{206}\text{Pb}/^{204}\text{Pb}$	$^{207}\text{Pb}/^{204}\text{Pb}$	$^{208}\text{Pb}/^{204}\text{Pb}$	$(^{206}\text{Pb}/^{204}\text{Pb})_i$	$(^{207}\text{Pb}/^{204}\text{Pb})_i$	$(^{208}\text{Pb}/^{204}\text{Pb})_i$
1	DY-7	Garwa	18.32	15.71	39.35	18.28	15.71	39.24
1	DC2	Garwa	18.36	15.66	39.22	18.35	15.66	39.15
1	D509	Garwa	18.40	15.69	39.13	18.38	15.69	39.08
1	DG43	Garwa	18.37	15.68	39.42	18.34	15.68	39.21
2	YE51	Yaqian	18.40	15.72	39.23	18.38	15.72	39.15
2	YC08	Yaqian	18.40	15.75	39.36	18.39	15.75	39.32
2	YG13	Yaqian	18.38	15.74	39.37	18.37	15.74	39.33
2	YF12	Yaqian	18.42	15.75	39.44	18.41	15.75	39.41
2	YA32	Yaqian	18.44	15.70	39.41	18.41	15.70	39.33
3	MH78	Mibale	18.49	15.75	39.58	18.46	15.75	39.52
3	MH69	Mibale	18.61	15.76	39.48	18.58	15.76	39.42
3	MG-3	Mibale	18.58	15.75	39.61	18.56	15.75	39.51
3	MY1	Mibale	18.54	15.78	39.62	18.52	15.78	39.55
3	MK09	Mibale	18.60	15.77	39.72	18.58	15.77	39.68
3	MR21	Mibale	18.63	15.80	39.58	18.60	15.79	39.51
3	MA75	Mibale	18.57	15.73	39.85	18.54	15.73	39.78
3	MX5	Mibale	18.53	15.73	39.51	18.51	15.72	39.48
5	G8	Chazi	18.80	15.70	40.06	18.78	15.70	40.03
5	C10	Chazi	18.94	15.82	39.99	18.92	15.82	39.95
5	CV5	Chazi	18.86	15.83	39.63	18.85	15.82	39.60
5	C76	Chazi	18.96	15.84	39.19	18.94	15.84	39.12
5	CH4	Chazi	18.90	15.82	39.63	18.88	15.82	39.58
5	CH7	Chazi	18.88	15.75	39.61	18.84	15.75	39.52
5	C03	Chazi	18.76	15.78	39.48	18.74	15.78	39.43
5	CX38	Chazi	18.82	15.72	39.95	18.79	15.72	39.89
5	C25	Chazi	18.99	15.85	39.40	18.96	15.85	39.33

Field number refers to number of the volcanic field in Fig. 1

$\lambda_{\text{U}238} = 0.155125 \times 10^{-9} \text{ year}^{-1}$ ,  $\lambda_{\text{U}235} = 0.98485 \times 10^{-9} \text{ year}^{-1}$  and  $\lambda_{\text{Th}232} = 0.049475 \times 10^{-9} \text{ year}^{-1}$  (Steiger and Jager 1977)

Initial Pb isotopic ratios were calculated using the average ages of the volcanic fields (Table 1)

exchange columns with dilute HBr as eluant. The whole procedure blank is less than 1 ng. During the period of analysis, repeat analyses of the international standard NBS981 yielded  $^{204}\text{Pb}/^{206}\text{Pb} = 0.059003 \pm 0.000084$  ( $n = 6$ , 2 sigma) (the certified value is 0.058998),  $^{207}\text{Pb}/^{206}\text{Pb} = 0.91449 \pm 0.00017$  ( $n = 6$ ) (the certified value is 0.914598) and  $^{208}\text{Pb}/^{206}\text{Pb} = 2.16691 \pm 0.00097$  ( $n = 6$ ) (the certified value is 2.168099). Pb isotopic fractionations were corrected using correction factors based on replicate analyses of the international standard NBS981. The Pb isotopic data are presented in Table 5. Detailed sample preparation and analytical procedures for the Sr–Nd–Pb isotopic measurements follow those of Guo et al. (2005, 2006).

## Results

No single-zircon U–Pb ages have been published previously for the post-collisional magmatic rocks in the XDY

rift (Fig. 1). Sample G8 from Chazi yields a reasonably well-defined U–Pb age of  $11.70 \pm 0.15 \text{ Ma}$ , within the age range between 25 and 8 Ma previously reported (Table 1; Fig. 2).

All of the studied rocks have relatively high  $\text{SiO}_2$  (52.76–58.32 wt.%) and  $\text{Al}_2\text{O}_3$  (11.10–13.67 wt.%) contents, and high Mg numbers [=molar  $\text{Mg} \times 100 / (\text{Mg} + \text{Fe}^{2+}) = 69\text{--}81$ , calculated assuming  $\text{Fe}_2\text{O}_3/(\text{FeO} + \text{Fe}_2\text{O}_3) = 0.20$ ], MgO (5.9–10.8 wt.%) and Ni (143.52–418.36 ppm) contents (electronic supplementary material 1). They are thus relatively primitive compositions, minimizing the likelihood of significant shallow-level crustal contamination and magmatic differentiation. The whole-rock geochemical data (electronic supplementary material 1) indicate that all of the studied XDY rocks are ultrapotassic, with  $\text{K}_2\text{O} > 3 \text{ wt.}\%$ ,  $\text{MgO} > 3 \text{ wt.}\%$  and  $\text{K}_2\text{O}/\text{Na}_2\text{O}$  ratios ranging from 2.35 to 9.89 (wt.%), except for two samples (CX38 and C66) with  $\text{K}_2\text{O}/\text{Na}_2\text{O}$  less than 2.0 (1.86 and 1.97). The latter two samples are considered to be potassic based on the criteria of Foley et al. (1987). The

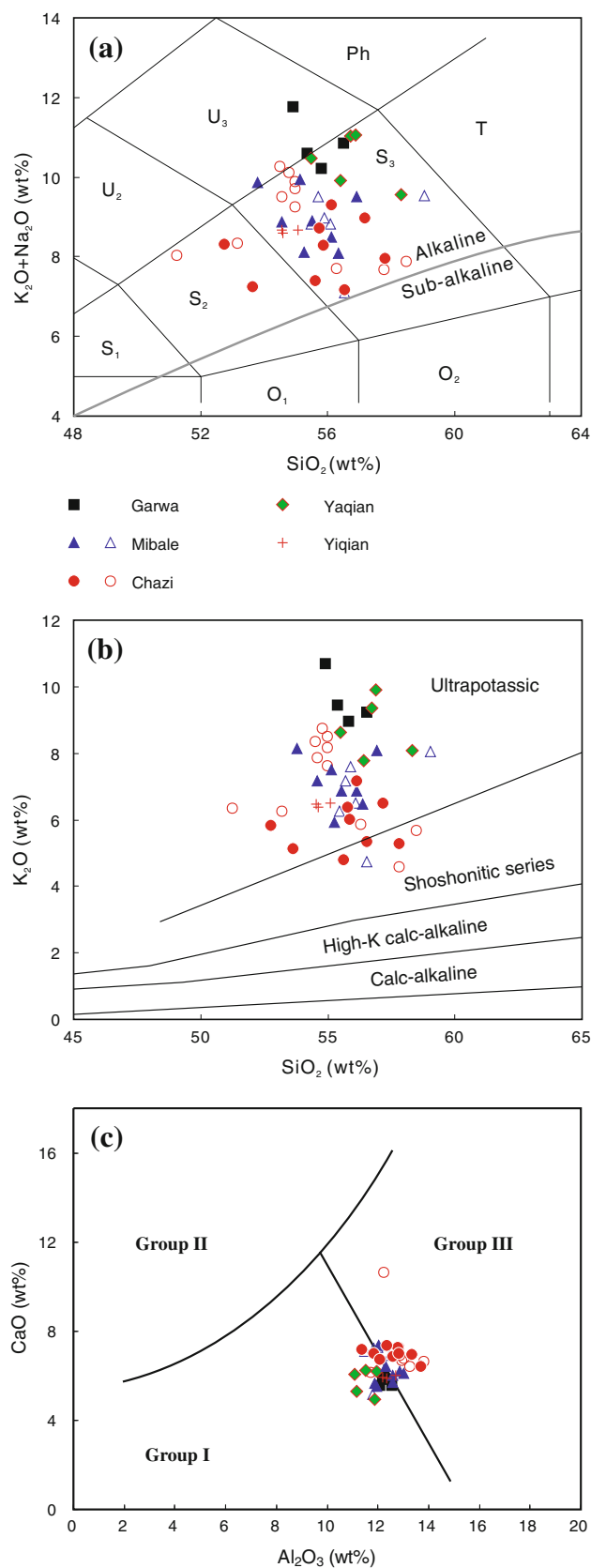


**Fig. 4** **a**  $K_2O + Na_2O$  (wt.%) versus  $SiO_2$  (wt.%) for the potassic and ultrapotassic igneous rocks of the XDY rift. All data plotted have been recalculated to 100 wt.% on a volatile-free basis (electronic supplementary material 1). Classification boundaries are from Le Bas et al. (1986) and Le Maitre et al. (1989). Filled and open symbols represent, respectively, data from this study and the published data of Liao et al. (2002), Ding et al. (2003, 2006), Gao et al. (2007), Chen et al. (2008) and Zhao et al. (2009). Fields marked by letters (in which the majority of the data plot) are as follows:  $S_2$ —basaltic trachyandesite,  $S_3$ —trachyandesite,  $U_3$ —tephriphonolite. **b**  $K_2O$  (wt.%) versus  $SiO_2$  (wt.%) diagram for the same samples plotted in **a**. Data have been normalized to 100 wt.% volatile-free as indicated in electronic supplementary material 1. The dividing lines show the classification boundaries from Rickwood (1989). Data sources and symbols are as in **a**. **c**  $CaO$  (wt.%) versus  $Al_2O_3$  (wt.%) classification diagram for the same samples plotted in **a**. Data have been normalized to 100 wt.% volatile-free as indicated in electronic supplementary material 1. The dividing lines show the classification boundaries from Foley et al. (1987). Data sources and symbols are as in **a**

compositions of the XDY rocks plotted in an  $Na_2O + K_2O$  versus  $SiO_2$  classification diagram lie almost totally within the tephriphonolite-basaltic trachyandesite–trachyandesite fields (Fig. 4a). A plot of  $K_2O$  versus  $SiO_2$  shows that most of the XDY rocks are ultrapotassic, although three samples plot in the shoshonitic series field (Fig. 4b). The major element oxide compositions of the XDY magmatic rocks (Fig. 4c) are transitional between Group I (anorogenic lamproites) and Group III (orogenic ultrapotassic rocks) according to the classification of Foley et al. (1987). The studied rocks have enriched light REE (LREE) and relatively flat heavy REE (HREE) profiles (chondrite-normalized  $La/Yb$  and  $Dy/Yb$  ratios are 33–225 and 1.64–3.48, respectively) and slightly negative Eu anomalies (Fig. 5). Similar REE patterns have been reported for lamproites from SE Spain (Nixon et al. 1984; Contini et al. 1993; Prelević et al. 2008; Conticelli et al. 2009) and central Italy (Rogers et al. 1985; Gasperini et al. 2002; Perini et al. 2004; Owen 2008; Boari et al. 2009; Conticelli et al. 2009). The studied rocks have steeper LREE patterns and weaker negative Eu anomalies in the northern part (i.e., rear-arc) than in the southern part (i.e., front-arc) of the XDY rift (Fig. 5). Some incompatible elements (e.g., Ba, Th, La) show an increasing trend, whereas trace element ratios (e.g.,  $Ba/La$ ,  $Th/Yb$ ,  $Th/Nd$ ) display a decrease from south to north within the rift (Figs. 6, 7). Primitive mantle-normalized incompatible trace element patterns (Fig. 6) are characterized by significantly negative Nb–Ta–Ti anomalies and pronounced positive anomalies in some large ion lithophile elements (LILE) (e.g., Rb, Pb, U and Th), despite the generally high contents of the elements Nb, Ta and Ti (electronic supplementary material 1). The incompatible trace element patterns are similar to those of lamproites from SE Spain (Venturelli et al. 1984; Prelević et al. 2008;

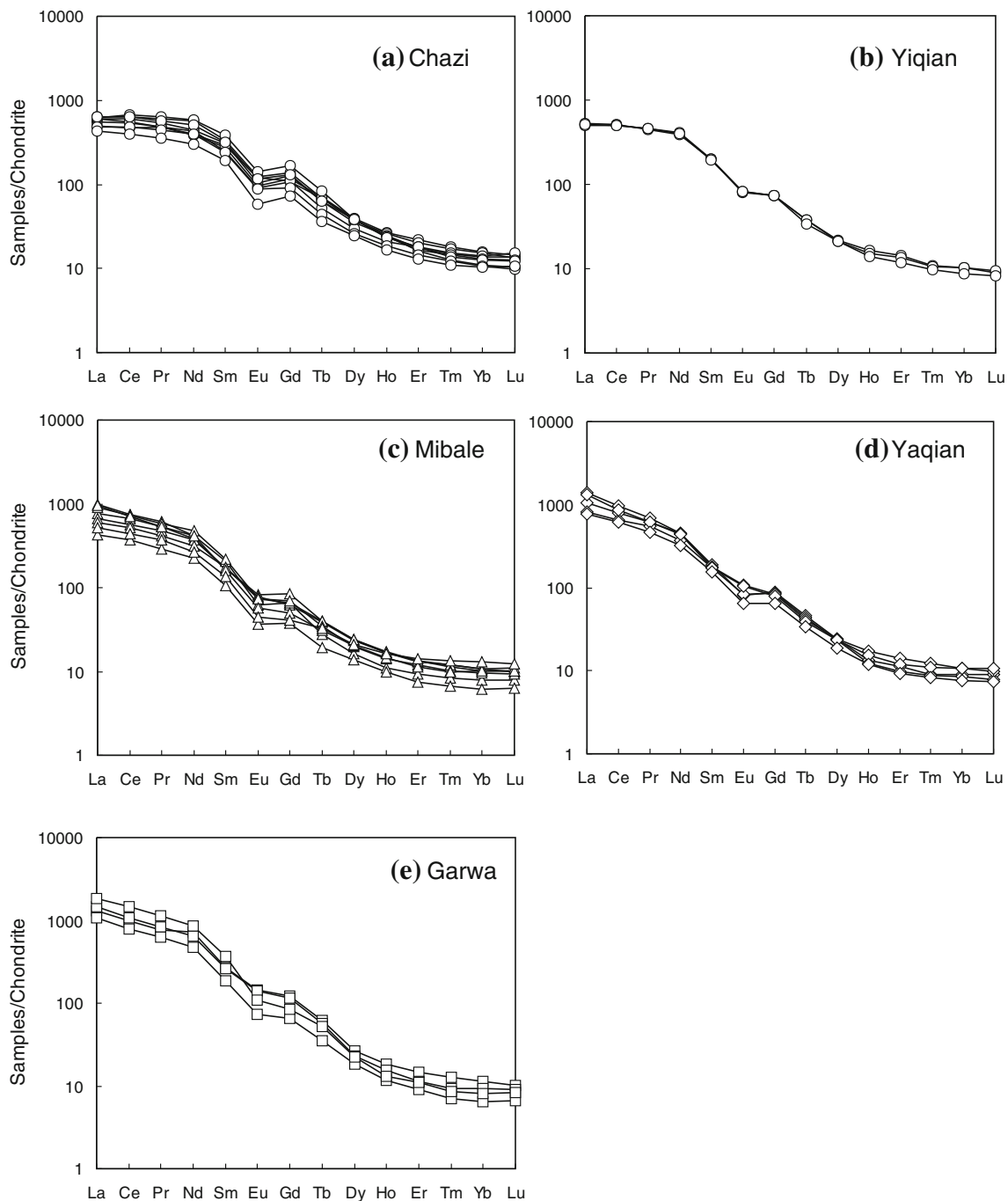


**Fig. 5** Chondrite-normalized rare earth element patterns for each of the volcanic fields of the XDY rift; normalization factors are from Sun and McDonough (1989). Data sources are as in Fig. 4a. **a** Chazi; **b** Yiqian; **c** Mibale; **d** Yaqian; **e** Garwa

Conticelli et al. 2009) and central Italy (Conticelli and Peccerillo 1992; Gasperini et al. 2002; Conticelli et al. 2009), which formed during the same orogenic cycle further to the west.

The XDY rift samples studied have high radiogenic ( $^{87}\text{Sr}/^{86}\text{Sr}$ )<sub>i</sub> (0.712600–0.736157) and low ( $^{143}\text{Nd}/^{144}\text{Nd}$ )<sub>i</sub> (0.511781–0.512046) relative to Bulk Earth, and high ( $^{207}\text{Pb}/^{204}\text{Pb}$ )<sub>i</sub> (15.661–15.846) and ( $^{208}\text{Pb}/^{204}\text{Pb}$ )<sub>i</sub> (39.086–40.023) at a given ( $^{206}\text{Pb}/^{204}\text{Pb}$ )<sub>i</sub> (18.280–18.957)

compared to the Northern Hemisphere Reference Line (NHRL; Hart 1984) (Fig. 8). The Sr–Nd–Pb isotopic ratios of the XDY rocks are similar to those of the lamproites from SE Spain (Nelson 1992; Prelević et al. 2008; Conticelli et al. 2009) and central Italy (Gasperini et al. 2002; Perini et al. 2004; Owen 2008; Boari et al. 2009; Conticelli et al. 2009). The data exhibit strong linear correlations falling almost exclusively between MORB-source mantle

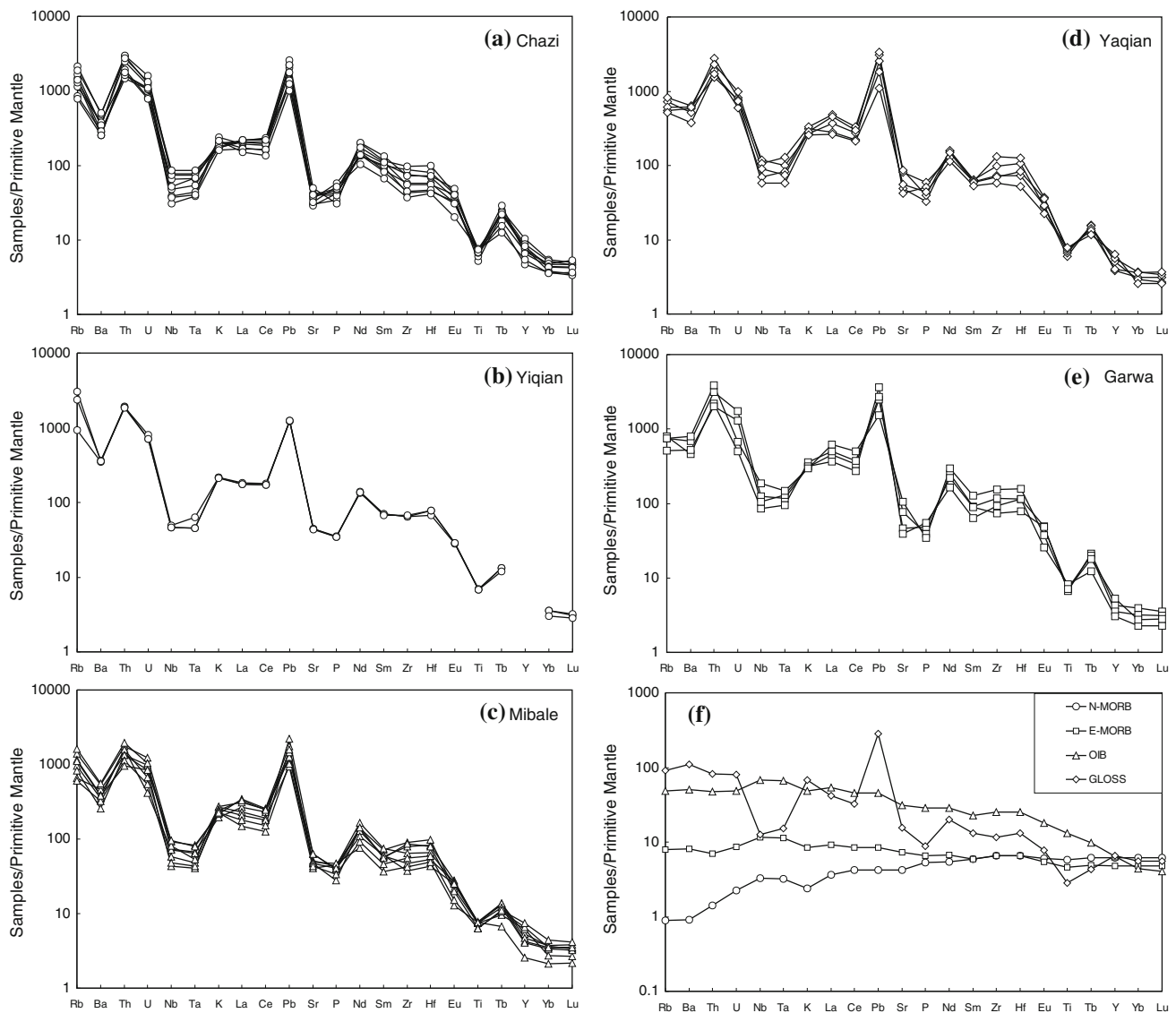


**Fig. 6** Primitive mantle-normalized trace element diagrams for each of the volcanic fields in the XDY rift; normalization factors are from Sun and McDonough (1989). Data sources are as in Fig. 4a. **a** Chazi;

**b** Yiqian; **c** Mibale; **d** Yaqian; **e** Garwa; **f** GLOSS (Plank and Langmuir 1998), OIB, N-MORB and E-MORB (Sun and McDonough 1989)

and Indian continental margin sediments [proxied by the isotopic composition of the Higher Himalayan Crystalline Sequence (HHCS); see Pan et al. (2004) and Richards et al. (2005) and references therein for more detailed discussion] in the Sr–Nd–Pb isotope diagrams (Fig. 8). From south (front-arc) to north (rear-arc) along the XDY rift, there is a general increase in  $^{143}\text{Nd}/^{144}\text{Nd}$  and a decrease in Sr and Pb isotopic ratios (Figs. 7, 8).

## Discussion

Previous studies on the post-collisional K-rich igneous rocks in south Tibet have provided important constraints on

the tectonic evolution of the Tibetan Plateau (e.g., Coulon et al. 1986; Turner et al. 1996; Miller et al. 1999; Williams et al. 2001, 2004; Ding et al. 2003; Nomade et al. 2004; Gao et al. 2007; Chen et al. 2010). Their major and trace element characteristics and Sr–Nd–Pb isotopic compositions provide insights into the nature of the mantle source region, partial melting processes, the geodynamic setting of the magmatism and plateau uplift mechanism.

Age trend of the post-collisional, K-rich magmatism in the XDY rift

To study the geodynamic setting of the post-collisional, K-rich magmatism in the XDY rift of south Tibet (Fig. 1),

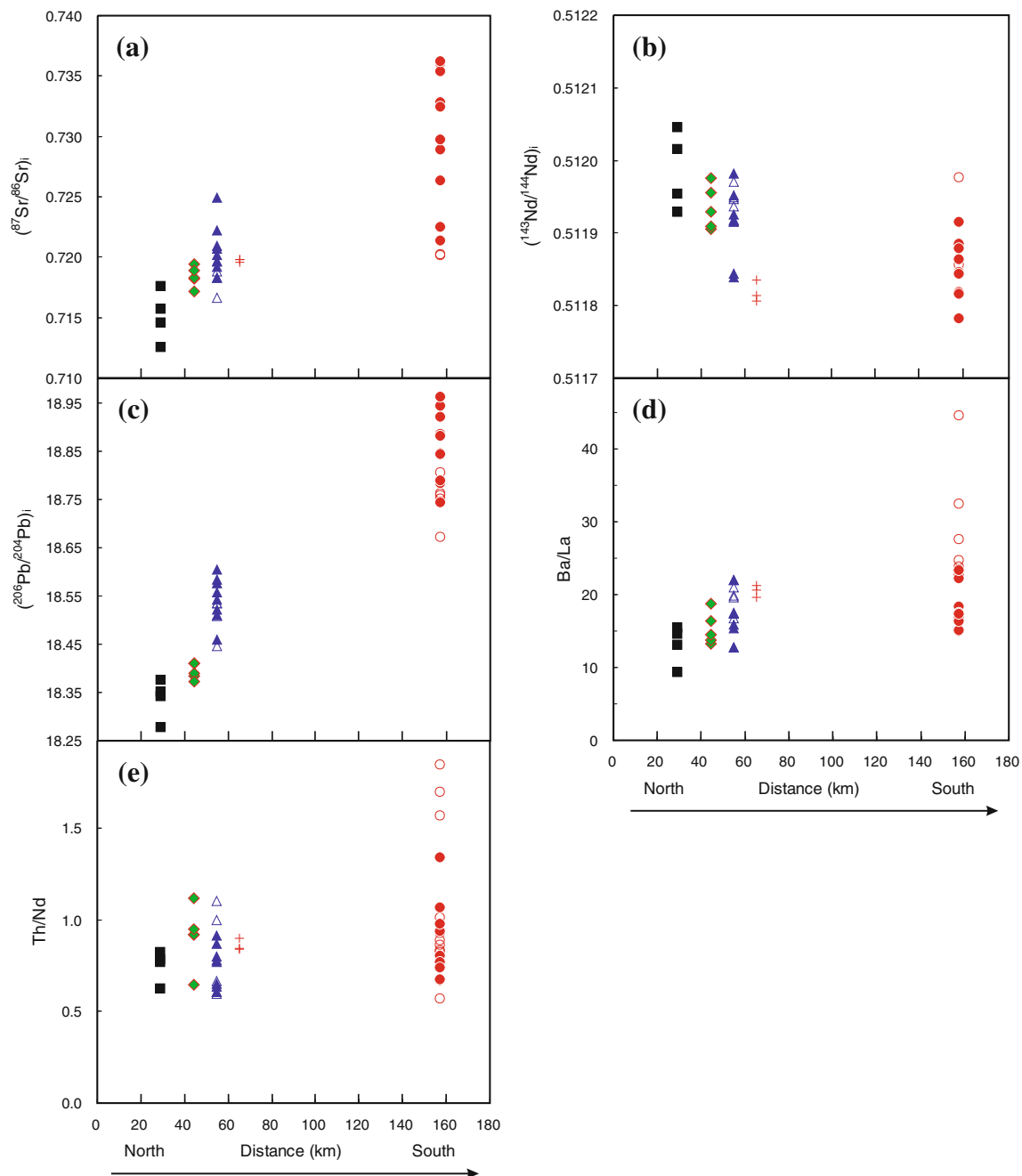


**Fig. 7** Sr–Nd–Pb isotopic and trace element ratios versus distance of the volcanic fields from Wenbu from north to south in the XDY rift in Fig. 1. **a**  $(^{87}\text{Sr}/^{86}\text{Sr})_i$ ; **b**  $(^{143}\text{Nd}/^{144}\text{Nd})_i$ ; **c**  $(^{206}\text{Pb}/^{204}\text{Pb})_i$ ; **d** Ba/La;

we have compiled all the available geochronological data from the published literature (Table 1). Several dating methods (e.g.,  $^{40}\text{Ar}/^{39}\text{Ar}$ ; K–Ar) have been used to date the magmatic rocks (Table 1). We have checked the data quality and compared the ages from the different methods to constrain the age ranges of the magmatic rocks. We also carried out additional zircon U–Pb dating for the magmatic rocks of the Chazi volcanic field as part of this study (Fig. 3; Table 3). Our data, together with the literature data, indicate a southward

**e** Th/Nd. The data of the K-rich magmatic rocks are from electronic supplementary material 1, Tables 4 and 5

decreasing trend in the age of the magmatism from 23 to 8 Ma in the rift (Fig. 2; Table 1).

Nature of the mantle source of the mafic K-rich magmas

*Three end-member components in the mantle source*

Oceanic basalts [i.e., ocean island basalts (OIB) and mid-ocean ridge basalts (MORB)] typically display positive

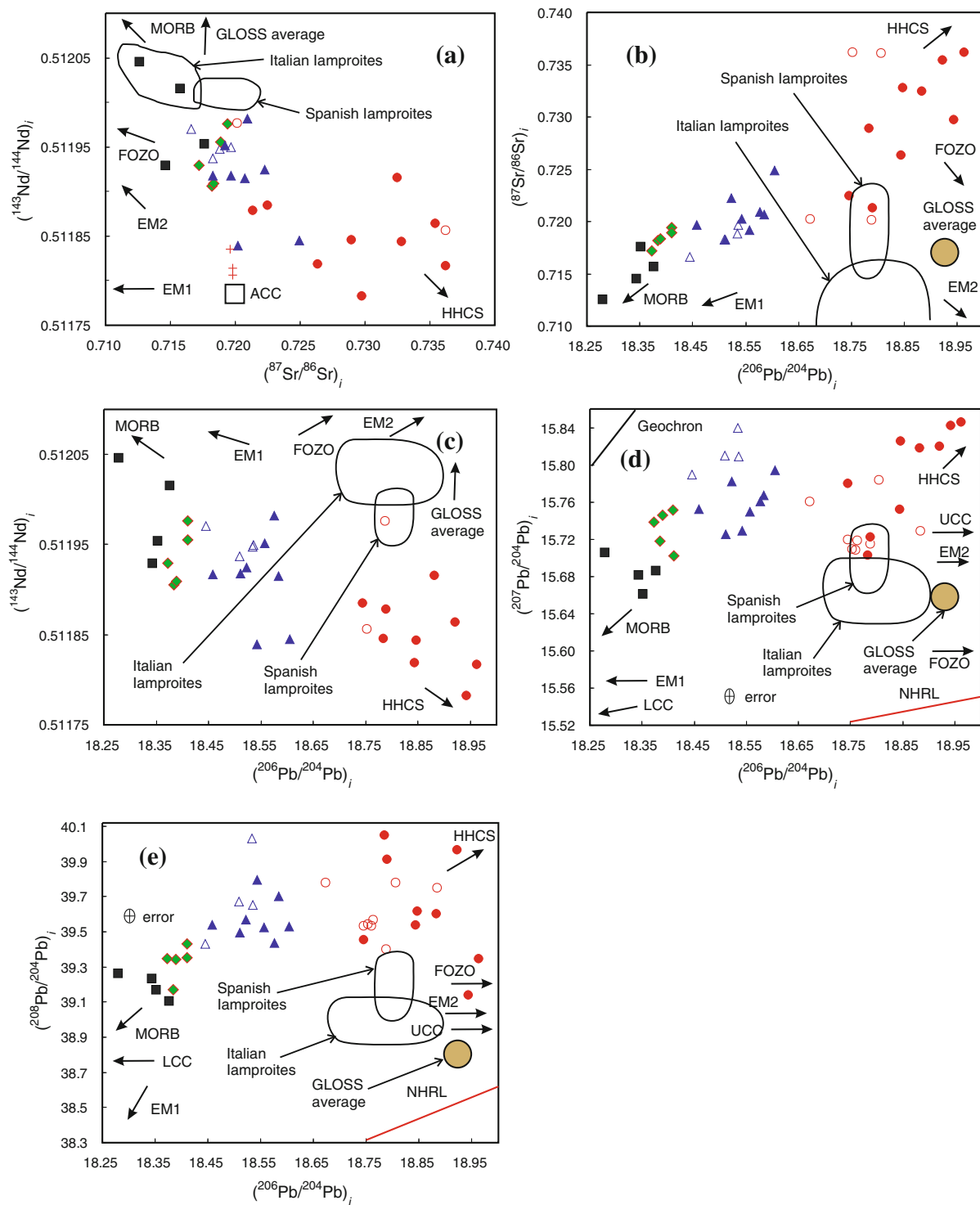


**Fig. 8** **a**  $(^{143}\text{Nd}/^{144}\text{Nd})_i$  versus  $(^{87}\text{Sr}/^{86}\text{Sr})_i$ . **b**  $(^{87}\text{Sr}/^{86}\text{Sr})_i$  versus  $(^{206}\text{Pb}/^{204}\text{Pb})_i$ . **c**  $(^{143}\text{Nd}/^{144}\text{Nd})_i$  versus  $(^{206}\text{Pb}/^{204}\text{Pb})_i$ . **d**  $(^{207}\text{Pb}/^{204}\text{Pb})_i$  versus  $(^{206}\text{Pb}/^{204}\text{Pb})_i$ . **e**  $(^{208}\text{Pb}/^{204}\text{Pb})_i$  versus  $(^{206}\text{Pb}/^{204}\text{Pb})_i$ . Arrows point toward the composition of MORB (Workman and Hart 2005) and the HHCS (Inger and Harris 1993; Ahmad et al. 2000; Richards et al. 2005; Guo and Wilson 2012). The Northern Hemisphere Reference Line (NHRL) is shown for reference (Hart 1984). Data for FOZO (common components of mantle plumes), average continental

crust (ACC), upper continental crust (UCC) and lower continental crust (LCC) are from Hofmann (1997). Average compositions for EM1, EM2 and GLOSS are from Zindler and Hart (1986), Hofmann (1997) and Plank and Langmuir (1998). Fields of Italian and Spanish lamproites are from Gasperini et al. (2002), Perini et al. (2004), Owen (2008), Prelević et al. (2008), Boari et al. (2009) and Conticelli et al. (2009). Data are from Tables 4 and 5. Symbols are as in Fig. 4a

Nb–Ta–Ti anomalies and negative Pb anomalies in primitive mantle-normalized incompatible trace element diagrams (e.g., Hofmann 1997). In contrast, the ultrapotassic and potassic mafic magmatic rocks from the XDY rift exhibit strongly negative Nb–Ta–Ti anomalies and positive Pb anomalies (Fig. 6), indicating that they were not derived from normal MORB- or OIB-source mantle. Contrasts in the Sr–Nd–Pb isotopic compositions of the XDY K-rich igneous rocks and oceanic basalts (MORB + OIB) support this inference (Fig. 8). Moreover, the Ce/Pb (1.82–8.24) and Nb/U (0.94–9.40) ratios of the XDY rift magmatic rocks are considerably lower than those of oceanic basalts (OIB and MORB) ( $\sim 25$  and  $\sim 47$ ; Hofmann 1988, 1997), also suggesting that they are not derived from normal asthenospheric mantle. High ( $^{87}\text{Sr}/^{86}\text{Sr}$ )<sub>i</sub> and low ( $^{143}\text{Nd}/^{144}\text{Nd}$ )<sub>i</sub> compared to oceanic basalts indicate a long-term enrichment of Rb over Sr and Nd over Sm in the mantle source region (Fig. 8). The high abundances of LILE (Rb, Ba and Sr), Th, U and Pb, and LREE (Figs. 5, 6) are consistent with this enrichment. Thus, we conclude that parental magmas of the XDY magmatic rocks were derived from an enriched mantle source rather than from normal asthenospheric mantle (cf MORB-source mantle).

Previous studies (e.g., Gill 1981; Pearce 1982; Tatsumi et al. 1986; Pearce and Parkinson 1993; Keppler 1996; Hawkesworth et al. 1997; Elburg et al. 2002; Turner et al. 2003; Guo et al. 2006) have demonstrated that subduction-related magmas are characterized by significant enrichment in LILE (Rb, Ba, Sr), Pb and LREE relative to the HFSE (Nb, Ta, Zr, Hf) and HREE, with strongly negative Nb–Ta–Ti anomalies and positive Pb anomalies in primitive mantle-normalized incompatible trace element diagrams. These characteristics are also shown by potassium-rich, mafic magmatic rocks from the XDY rift (Fig. 6). Their Sr–Nd–Pb isotopic compositions display a linear trend between the ambient asthenospheric mantle (MORB-source mantle) and subducted sediments likely derived from erosion of the HHCS (Fig. 8), consistent with a subduction-related origin for the asthenospheric mantle source enrichment. The HHCS is composed of Paleoproterozoic to Ordovician (500–600 Ma) high-grade metasedimentary rocks, comprising amphibolite-grade schists, gneisses, migmatites and calc-silicates intruded by Paleozoic and Miocene granites (Pan et al. 2004; Richards et al. 2005). The HHCS forms the high-grade metamorphic crystalline basement in the Himalayan orogen of northern India (Pan et al. 2004; Richards et al. 2005). The presence of a northward subducted Indian continental lithosphere slab beneath the XDY rift, based on seismic tomographic studies (e.g., Li et al. 2008; Zhao et al. 2010, 2011), supports this inference.

Previous studies (e.g., Elburg et al. 2002; Guo et al. 2006) have indicated that enrichment of the asthenospheric

mantle wedge above a subducted slab of continental lithosphere can be broadly attributed to migration of (1) aqueous fluids derived from dehydration of subducted continental sediments and/or (2) melts derived from partial melting of the subducted continental lithosphere. Geochemical distinctions can be made between subduction-related magmatic rocks in which the magma source has been modified by subduction-related aqueous fluids and those in which the source is enriched by partial melts of the subducted slab (e.g., Hawkesworth et al. 1997; Class et al. 2000; Woodhead et al. 2001; Elburg et al. 2002; Guo et al. 2005; 2006). Aqueous fluids, which carry very little REE, Th and HFSE (e.g., Hf, Nb, Zr and Ta), introduce significant amounts of large ion lithophile elements (e.g., K, Rb, Ba and Sr) and other fluid-mobile trace elements (e.g., U, Pb) into the mantle wedge. However, partial melts of subducted continental margin sediments are characterized by relatively high Th, LILE and LREE contents. Thus, those subduction-related magmatic rocks whose source was strongly metasomatized by a fluid component are likely to have higher Ba/La, Ba/Th, U/Th and Sr/Th ratios than those rocks whose source was enriched by a partial melt of subducted continental sediments. In contrast, those subduction-related magmas with a strong imprint of a partial melt derived from the subducted continental lithosphere in their source region should have higher Th/Nd, Th/U, Th/Ba, Th/Sr and Th contents than those derived from a fluid-metasomatized mantle source. Magmas derived from both fluid- and melt-metasomatized sources should have Sr–Nd–Pb isotopic compositions between those of the subducted continental sediments and the normal asthenospheric mantle.

Previous studies (e.g., McCulloch and Gamble 1991; Plank and Langmuir 1998; Class et al. 2000; Elburg et al. 2002; Guo et al. 2005) have indicated that the HFSE (Nb, Ta, Zr and Hf) are unlikely to be transferred from the subducted slab to the mantle wedge by the enriched components (fluids or melts) derived from the subducted slab, because of their insolubility in subduction fluids and depletion in slab-melts controlled by the stability of residual Ti-bearing phases (e.g., rutile, titanite and Ti-magnetite). Thus, the HFSE ratios (e.g., Nb/Ta, Zr/Hf; Fig. 9) in the mafic K-rich rocks of the XDY rift are likely to be close to those of the mantle wedge prior to modification by the subduction-derived components (fluids and melts). Nb/Ta and Zr/Hf ratios in the XDY rift magmatic rocks are similar to those of MORB (Fig. 9), indicating that the mantle wedge prior to modification by the subduction-derived components (fluids and melts) is more like MORB-source mantle rather than OIB-source mantle.

Woodhead et al. (2001) demonstrated that ratios of fluid-mobile trace elements to fluid-immobile trace elements may effectively reflect the importance of subduction

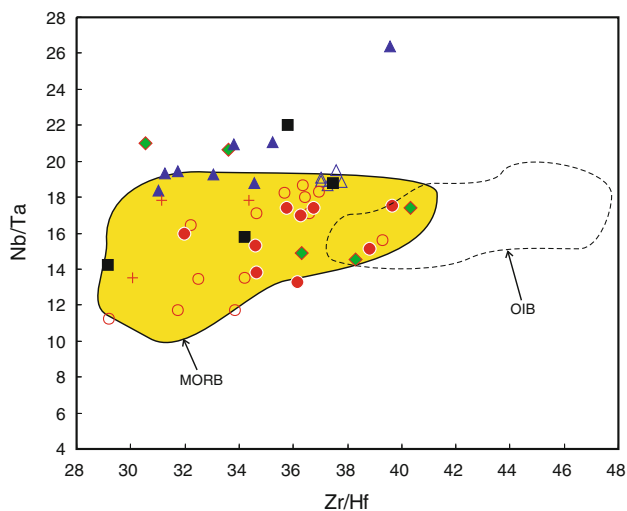


**Fig. 9** Nb/Ta versus Zr/Hf for the K-rich volcanic rocks of the XDY rift. Data are from electronic supplementary material 1. The *sample symbols* are as in Fig. 4a. *Arrows* labeled “MORB” and “OIB” point toward the field of composition of mid-ocean ridge basalts (MORB) and ocean island basalts (OIB), respectively. Data sources are as follows: MORB (Sun and McDonough 1989; Workman and Hart 2005; Pfänder et al. 2007) and OIB (Sun and McDonough 1989; Pfänder et al. 2007)

fluids in the mantle source of subduction-related magmas. We use the ratio of the fluid-mobile element Ba to fluid-immobile La to constrain the involvement of subduction fluids because the Ba/La ratio is insignificantly fractionated during partial melting. The high Ba/La ratios in the XDY rift magmatic rocks thus reflect the presence of slab-derived hydrous fluids in their mantle source region (Fig. 10a).

The combination of incompatible element and isotopic ratios has been effectively used as a fingerprint in identifying the origin of metasomatic components in the source of subduction-related magmas (Hawkesworth et al. 1997; Turner et al. 1997; Class et al. 2000; Guo et al. 2005, 2006). The XDY rift mafic K-rich rocks define a broadly linear trend in a plot of  $(^{143}\text{Nd}/^{144}\text{Nd})_i$  versus Ba/La (Fig. 10b); this array may be explained by a two-end-member mixing process in their mantle source region. One end-member has similar  $(^{143}\text{Nd}/^{144}\text{Nd})_i$  (0.513106; for the detailed calculations, see Table 6 and Workman and Hart 2005) and Ba/La (2.93; Workman and Hart 2005) to MORB, which may indicate the background composition of the mantle wedge prior to modification by the subduction-derived components; the other end-member has a comparable  $(^{143}\text{Nd}/^{144}\text{Nd})_i$  to that of the HHCS, but its Ba/La is much higher than the bulk HHCS (Fig. 10b), precluding the possibility that the bulk HHCS acts as the end-member. This second end-member in the mantle source of the XDY rift magmatic rocks is thus more likely a subducted HHCS-derived fluid, because of the more strongly mobile nature of Ba than La in subduction fluids.

Th is more incompatible than Nd during partial melting under subduction zone conditions (Johnson and Plank 1999). Thus, only a partial melt derived from subducted sediments can fractionate the Th/Nd ratio from that of the bulk sediments because of the fluid-immobile nature of Th and Nd. High Th/Nd ratios indicate the presence of slab-derived partial melts in the mantle source of the XDY rift magmatic rocks (Fig. 10a). The magmatic rocks define a two-end-member mixing array between MORB- and HHCS-derived partial melts in a plot of  $(^{143}\text{Nd}/^{144}\text{Nd})_i$  versus Th/Nd (Fig. 10c), indicating that the mantle source of the XDY rift magmas was metasomatized by partial melts of subducted HHCS sediments as a consequence of the northward underthrusting of the Indian continental lithosphere beneath Tibet.

Based on the combined constraints of trace element ratios and Sr–Nd–Pb isotopic compositions (Figs. 8, 9, 10), we conclude that the mantle source of the XDY rift magmas in south Tibet resulted from metasomatism of MORB-source mantle by both fluids and melts derived from the subducted HHCS; the three end-member components in the mantle source are MORB-source mantle, slab-derived fluid and slab-derived melt. From the frontal arc (south) to the back-arc (north) of the XDY rift, the ratios of Ba/La and Th/Nd decrease (Fig. 10a), suggesting a decreasing trend in the proportion of fluid and melt in the mantle source. On the basis of these three end-member components, we model the Sr–Nd–Pb isotopic compositions of the XDY rift magmatic rocks by the addition of both a fluid and a partial melt derived from subducted HHCS sediments to a MORB-source mantle wedge beneath south Tibet.

#### *Proportions of the three end-member components in mantle source*

To calculate the proportions of metasomatic components (fluid and melt) derived from the subducted HHCS in the mantle source of the XDY rift magmatic rocks, we carried out Sr–Nd–Pb isotopic three-component mixing model simulations (Fig. 11). Using the calculation techniques of Elburg et al. (2002) and Guo and Wilson (2012), we estimated the trace element contents and Sr–Nd–Pb isotopic ratios of the three end-members (fluid, melt and MORB-source mantle wedge) in the mantle source (Table 6), based on solid–fluid (and solid–melt) experimental partitioning of trace elements in subducted sediments (Johnson and Plank 1999). On the basis of our previous model calculations (Guo and Wilson 2012), we selected the original bulk-rock composition of a biotite paragneiss as a proxy for the bulk composition of the HHCS in our isotopic mixing model simulation because it is an easily fusible lithology within the HHCS (Richards et al. 2005). The calculation process for the Sr–Nd–Pb isotopic three-component mixing model

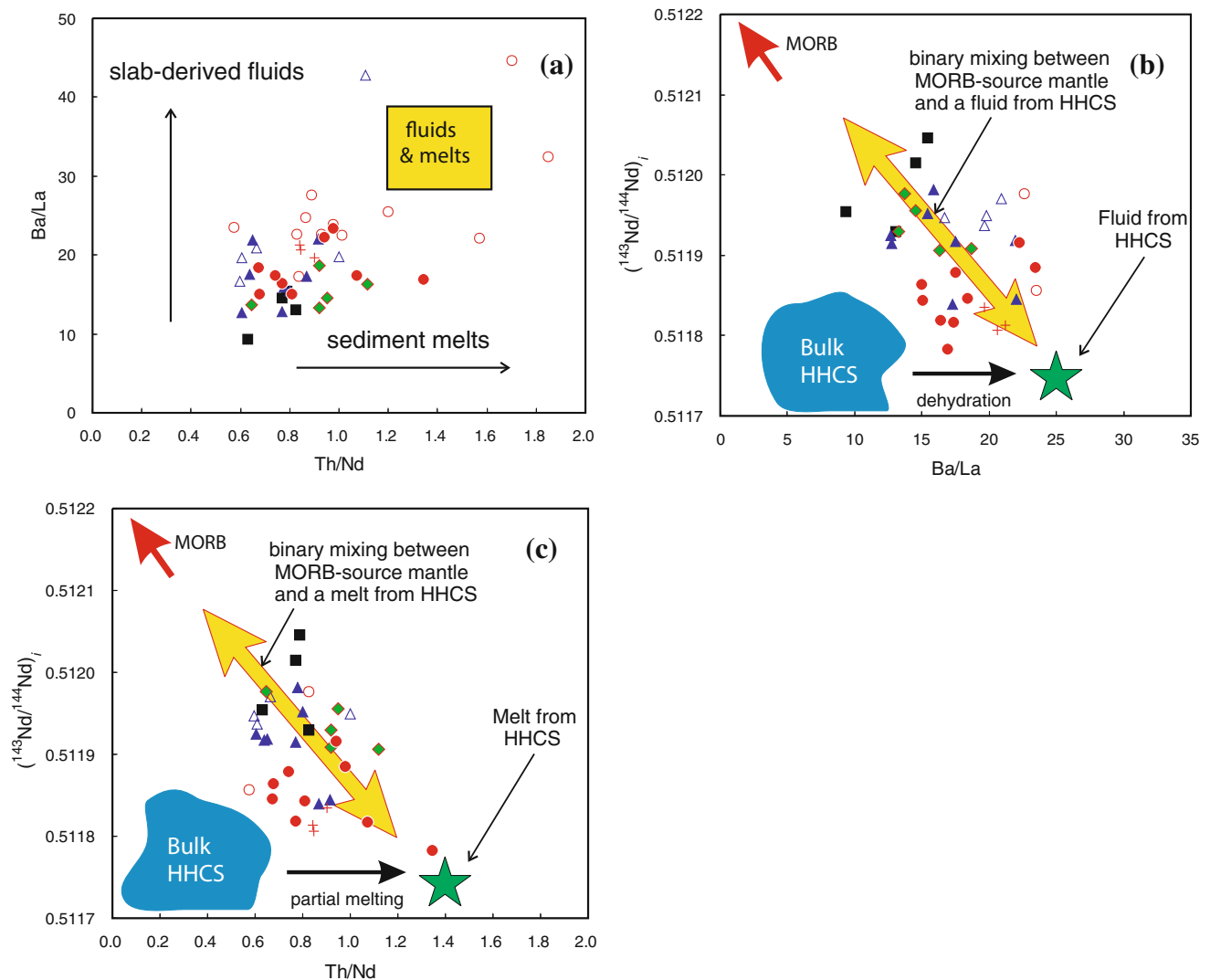


**Fig. 10** **a** Ba/La versus Th/Nd. **b**  $(^{143}\text{Nd}/^{144}\text{Nd})_i$  versus Ba/La. **c**  $(^{143}\text{Nd}/^{144}\text{Nd})_i$  versus Th/Nd. The XDY rift K-rich magmatic rocks form linear arrays, consistent with binary mixing between MORB-source mantle and components with higher Ba/La and Th/Nd ratios than the bulk HHCS in **b** and **c**, respectively. These components may be explained as a fluid in **b** and melt in **c** derived from the HHCS (for more details see the main text). All data plotted are from electronic supplementary material 1 and Table 4. The symbols are as in Fig. 4a. The arrows labeled “slab-derived fluids” and “sediment melts” in **a** indicate the trends of compositional changes due to the addition of slab-derived fluids and melts, respectively. The yellow-filled rectangle labeled “fluids and melts” in **a** denotes the compositional characteristics of slab-derived fluids and melts. The red bold arrows labeled “MORB” indicate the composition of MORB, and the blue-filled

fields labeled “Bulk HHCS” show the composition of bulk HHCS in **b** and **c**. The green-filled stars represent the composition of HHCS-derived fluid and HHCS-derived melt in **b** and **c**, respectively. Bold black arrows labeled “dehydration” and “partial melting” indicate the direction of compositional changes of components caused by dehydration and partial melting of the bulk HHCS in **b** and **c**, respectively. The yellow-filled arrows in **b** indicate binary mixing between the MORB-source mantle and a fluid derived from the HHCS, whereas the yellow-filled arrows in **c** indicate binary mixing between the MORB-source mantle and a partial melt derived from the HHCS. Data sources are as follows: Composition of MORB (Sun and McDonough 1989; Workman and Hart 2005) and HHCS (Inger and Harris 1993; Ahmad et al. 2000; Richards et al. 2005; Guo and Wilson 2012)

follows that of Faure and Mensing (2005). The results of the calculation are shown in Fig. 11 and Table 6.

The Sr–Nd–Pb isotopic three-component mixing calculation results indicate that the proportion of slab fluid and slab melt in the mantle source of the XDY rift K-rich magmatic rocks are 0–5 % and 2.0–15 %, respectively (Fig. 11; Table 6). The amount of the fluid and melt

derived from the subducted HHCS in the mantle source increases from north to south within the rift (Figs. 1, 11). This is supported by the more continental (i.e., more radiogenic Sr and Pb isotopic and less radiogenic Nd isotopic compositions) isotopic characteristics of the K-rich rocks in the south than in the north of the rift (Figs. 7, 8). Additionally, the stronger negative Eu and Sr anomalies in

**Table 6** Sr–Nd–Pb isotopic three-component mixing model calculation results, (1) the first-step mixing between MORB-source mantle wedge and a fluid derived from subducted HHCS, (2) a second-step

mixing between the fluid-modified mantle wedge and a partial melt from dehydrated HHCS

HHCS-derived fluid (%)	0 %	0.5 %	1 %	2 %	3 %	5 %	10 %
(1)							
$(^{87}\text{Sr}/^{86}\text{Sr})_{M1}$	0.702626	0.706162	0.709148	0.713912	0.717545	0.722719	0.729784
$(^{143}\text{Nd}/^{144}\text{Nd})_{M1}$	0.513106	0.512897	0.512742	0.512526	0.512384	0.512207	0.512005
$(^{206}\text{Pb}/^{204}\text{Pb})_{M1}$	18.249	18.451	18.577	18.726	18.812	18.905	18.999
(2)							
(a) Garwa and Yaqian (fluid = 0 %; melt = 2–5 %)							
$(^{87}\text{Sr}/^{86}\text{Sr})_{M2}$	0.702626	0.705994	0.708862	0.713486	0.717052	0.72219	0.729321
$(^{143}\text{Nd}/^{144}\text{Nd})_{M2}$	0.513106	0.512716	0.512496	0.512257	0.512129	0.511995	0.511867
$(^{206}\text{Pb}/^{204}\text{Pb})_{M2}$	18.249	18.269	18.289	18.326	18.361	18.424	18.550
(b) Mibale and Yiqian (fluid = 0.5 %; melt = 3–10 %)							
$(^{87}\text{Sr}/^{86}\text{Sr})_{M2}$	0.706162	0.708992	0.711434	0.715435	0.718575	0.723188	0.729767
$(^{143}\text{Nd}/^{144}\text{Nd})_{M2}$	0.512897	0.512603	0.512425	0.512221	0.512108	0.511985	0.511864
$(^{206}\text{Pb}/^{204}\text{Pb})_{M2}$	18.451	18.463	18.475	18.497	18.519	18.559	18.644
(c) Chazi (fluid = 2–5 %; melt = 3–15 %) (The following data shown is result when fluid is 3 % in the source)							
$(^{87}\text{Sr}/^{86}\text{Sr})_{M2}$	0.717545	0.718941	0.720201	0.722382	0.724206	0.727084	0.731655
$(^{143}\text{Nd}/^{144}\text{Nd})_{M2}$	0.512384	0.512277	0.512199	0.512094	0.512026	0.511943	0.51185
$(^{206}\text{Pb}/^{204}\text{Pb})_{M2}$	18.812	18.814	18.817	18.822	18.827	18.837	18.860

$(^{87}\text{Sr}/^{86}\text{Sr})_M$ ,  $(^{143}\text{Nd}/^{144}\text{Nd})_M$  and  $(^{206}\text{Pb}/^{204}\text{Pb})_M$  are the initial isotopic ratios of Sr, Nd and Pb calculated using the three-component mixing model.  $M$  in the subscript represents the calculation value by the Sr–Nd–Pb isotopic mixing modeling. The expression of the Sr–Nd–Pb isotopic three-component mixing model follows that of Faure and Mensing (2005)

Based on the previous studies (Inger and Harris 1993; Ahmad et al. 2000; Richards et al. 2005), we considered a fluid and a melt derived from biotite gneiss within the Higher Himalayan Crystalline Sequence (HHCS) to represent the compositions of the two mixing end-members in the mantle source of the XDY magmas. The composition of the bulk biotite gneiss within the HHCS is as follows (Inger and Harris 1993; Richards et al. 2005): Sr = 135.0 ppm;  $(^{87}\text{Sr}/^{86}\text{Sr})_i = 0.742355$ ; Nd = 29.9 ppm;  $(^{143}\text{Nd}/^{144}\text{Nd})_i = 0.511725$ ; Pb = 40.0 ppm;  $(^{206}\text{Pb}/^{204}\text{Pb})_i = 19.11$ . On the basis of the above data, following the approach of Guo et al. (2005, 2006), Sr, Nd and Pb concentrations in the fluid and melt derived from the subducted HHCS were estimated for the Sr–Nd–Pb isotopic three-component mixing model calculations, using solid–fluid (and solid–melt) experimental partitioning of these trace elements in subduction environments (Johnson and Plank 1999). The estimated Sr, Nd and Pb concentrations are 149.01, 20.59 and 48.78 ppm in the HHCS-derived fluid, and 141.28, 45.45 and 3.87 ppm in the partial melt of already dehydrated HHCS, respectively

We considered the depleted MORB mantle (DMM) of Workman and Hart (2005) to represent the composition of the third mixing end-member (i.e., the background of the mantle wedge prior to modification by the subduction-derived components). The composition of the MORB-source mantle wedge is as follows (Workman and Hart 2005): Sr = 7.664 ppm;  $(^{87}\text{Sr}/^{86}\text{Sr})_i = 0.702626$ ; Nd = 0.581 ppm;  $(^{143}\text{Nd}/^{144}\text{Nd})_i = 0.513106$ ; Pb = 0.018 ppm;  $(^{206}\text{Pb}/^{204}\text{Pb})_i = 18.249$

The initial ratios of  $(^{87}\text{Sr}/^{86}\text{Sr})_i$ ,  $(^{143}\text{Nd}/^{144}\text{Nd})_i$  and  $(^{206}\text{Pb}/^{204}\text{Pb})_i$  in the HHCS and mantle wedge are age-corrected to 15 Ma (average age of the post-collisional, K-rich magmatism in the XDY rift of south Tibet)

the south than in the north of the XDY rift (Figs. 5, 6) are consistent with an increasing proportion of the HHCS-derived melts in the source from north to south, because the HHCS metasediments have strong negative Eu and Sr anomalies.

#### Trace element modeling

The positive linear correlation between La/Yb and La (Fig. 12) indicates that partial melting is an important process in the generation of the compositional spectrum of the XDY rift mafic K-rich magmas. Together with the La/Yb increase with increasing La from south to north (Fig. 12), this indicates that the degree of melting of the

mantle source is higher in the south than that in the north of the rift (Fig. 1). The different slopes of the REE patterns of the individual volcanic fields from north to south (Figs. 5, 12) indicate a difference in their mantle source composition. In spite of this, the broadly positive trend between La/Yb and La (Fig. 12) suggests that the difference between the mantle source compositions of the individual volcanic fields in the XDY rift is insignificant and also that their source composition has an interlink from north to south. This is consistent with the inference based on the isotopic mixing calculations (Fig. 11).

To further simulate the magma generation process, we performed trace element modeling calculations using a non-modal batch melting model (Wilson 1989; Guo et al.

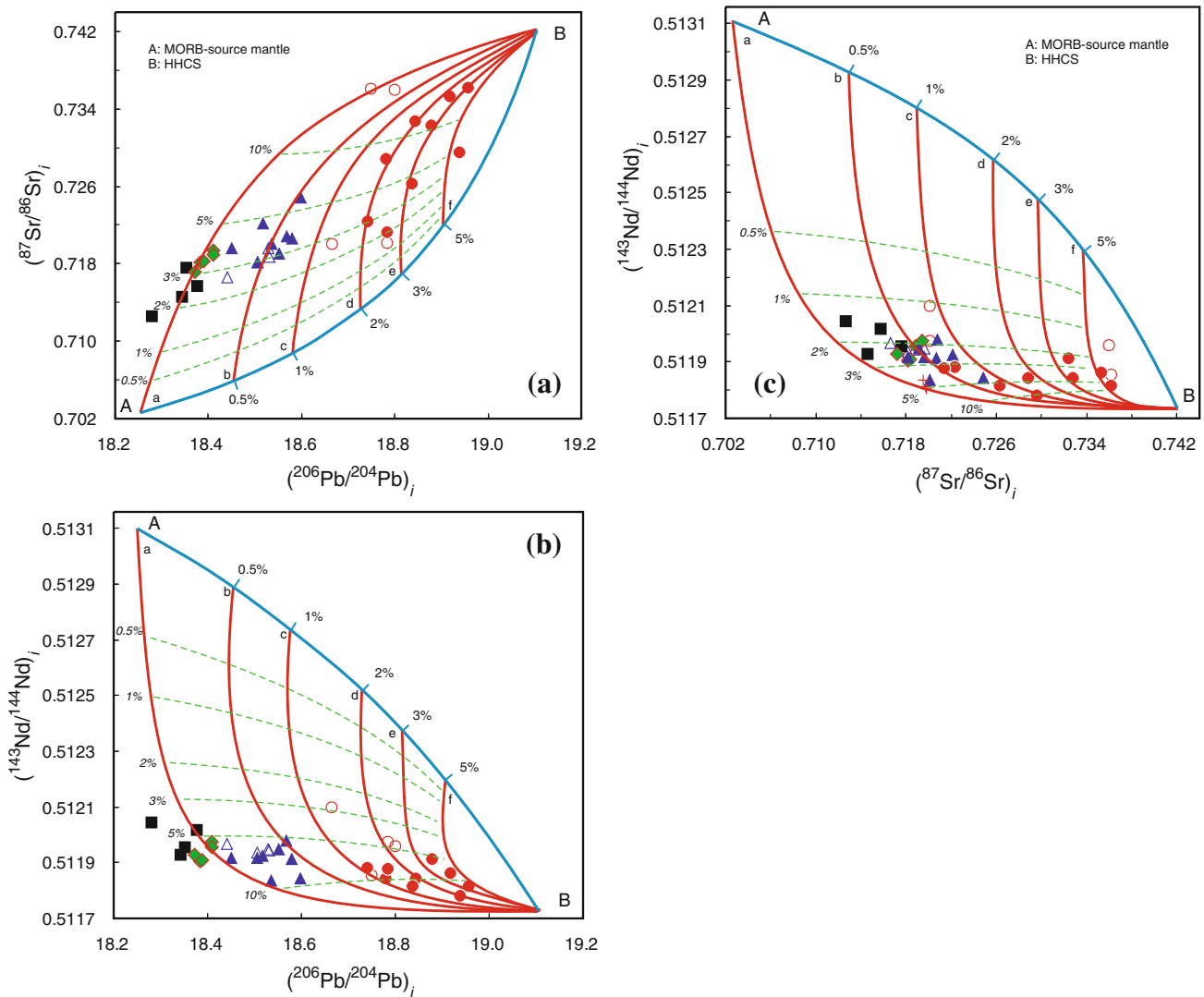


**Fig. 11** Comparison between the Sr–Nd–Pb isotopic compositions of the K-rich magmatic rocks from the XDY rift (Tables 4, 5) and our model isotope mixing curves. **a**  $(^{87}\text{Sr}/^{86}\text{Sr})_i$  versus  $(^{206}\text{Pb}/^{204}\text{Pb})_i$ . **b**  $(^{143}\text{Nd}/^{144}\text{Nd})_i$  versus  $(^{206}\text{Pb}/^{204}\text{Pb})_i$ . **c**  $(^{143}\text{Nd}/^{144}\text{Nd})_i$  versus  $(^{87}\text{Sr}/^{86}\text{Sr})_i$ . The Sr–Nd–Pb isotopic data for the K-rich magmatic rocks can be simulated by mixing between a HHCS-derived fluid and a MORB-source mantle component (blue curve with tick marks from A to B), followed by mixing of this fluid-modified mantle with a partial melt of dehydrated HHCS (red curves: B-a, B-b, B-c, B-d, B-e and B-f). The numbers in per cent shown on the tick marks of the blue curve from A to B denote the proportions of a fluid derived from the bulk HHCS in a two-component mixing model between MORB-

source mantle and a subducted HHCS-derived fluid. The numbers in percent (in italics) along the green dashed lines are the proportions of a melt in the metasomatized mantle source which has been enriched by both fluids and partial melts derived from the HHCS. The detailed calculation procedures are explained in the text and Table 6. The symbols for the XDY rift samples are as in Fig. 4a. A is MORB-source mantle (Sun and McDonough 1989; Workman and Hart 2005), and B is biotite gneiss (W6; Richards et al. 2005) from the HHCS.  $(^{87}\text{Sr}/^{86}\text{Sr})_i$ ,  $(^{143}\text{Nd}/^{144}\text{Nd})_i$  and  $(^{206}\text{Pb}/^{204}\text{Pb})_i$  data for the HHCS- and MORB-source mantle are age-corrected to 15 Ma (average age of the K-rich rocks studied)

2005, 2006; Guo and Wilson 2012). As noted earlier, the REE and incompatible trace element compositions of the XDY rift magmatic rocks may provide important constraints on the residual mineralogy of their mantle source region. For example, the relatively high HREE concentrations and slightly low  $(\text{Gd}/\text{Yb})_N$  ratios (where  $N$  in the subscript represents the chondrite-normalized value) of the XDY rift samples (e.g., Yb contents which are more than

10 times chondritic abundances; Fig. 5) preclude garnet as a residual mineral in the mantle source region. Instead, the REE patterns are consistent with the presence of spinel in the mantle source. The significantly negative Ta, Nb and Ti anomalies in the mantle-normalized trace element patterns are consistent with the presence of residual Ti-bearing phases (e.g., rutile and titanite) because these phases have high partition coefficients for the elements Ta, Nb and Ti

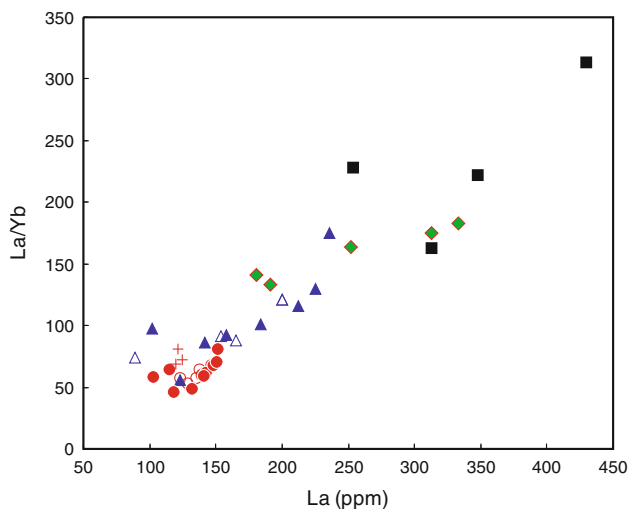


**Fig. 12** Variation of La/Yb versus La (ppm) for the K-rich magmatic rocks. Data sources and symbols are as in Fig. 4a

(Fig. 6). Previous studies (e.g., Furman and Graham 1999) have indicated that partial melts in equilibrium with residual phlogopite have higher Rb/Sr ( $>0.1$ ) and lower Ba/Rb ( $<20$ ) than those derived from an amphibole-bearing mantle source region. The low Ba/Rb and high Rb/Sr ratios in the K-rich rocks of the southern part of the XDY rift (Chazi) suggest the presence of residual phlogopite in the mantle source region, whereas the high Ba/Rb and low Rb/Sr ratios in the north of the rift (Garwa) are consistent with residual amphibole in the mantle source (Fig. 13). The strongly negative P anomalies in the mantle-normalized incompatible trace element patterns, combined with the flat LREE patterns of the K-rich rocks of the southern XDY

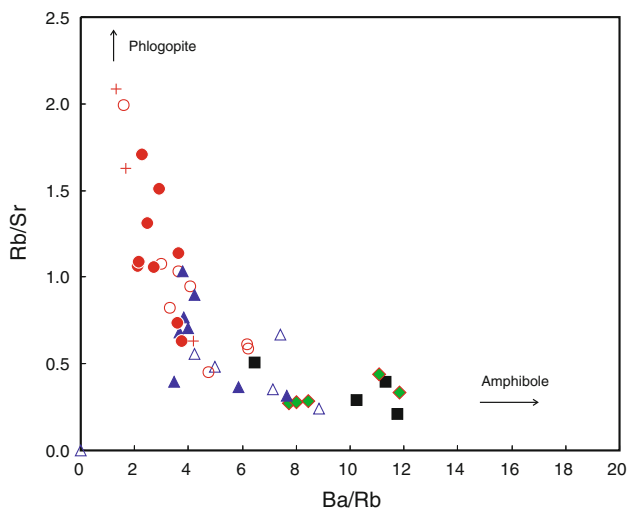


**Fig. 13** Variation of Rb/Sr versus Ba/Rb for the K-rich magmatic rocks. Amphibole and Phlogopite on the arrows refer to these phases as residual phases in the source region. Data sources and symbols are as in Fig. 4a

rift, are consistent with the additional presence of residual apatite in the mantle source region (Figs. 5, 6).

A number of studies have estimated the modal mineralogy of MORB-source wedge mantle. For example, Johnson (1998) and Hellebrand et al. (2002) indicated that in the spinel peridotite facies the mineral modes in MORB-source mantle are olivine (53 %), orthopyroxene (27 %), clinopyroxene (17 %) and spinel (3 %). Bizimis et al. (2000) proposed a similar modal mineralogy of olivine (55 %), orthopyroxene (25 %), clinopyroxene (18 %) and spinel (2 %). Infiltration of a subducted sediment-derived fluid or melt into the mantle source may change the above modal mineralogy and, in particular, would increase the content of orthopyroxene at the expense of olivine (Kelemen et al. 1998). In our study, the residual mineral assemblage in the mantle source of the XDY rift magmas is determined using an iterative calculation method (see below).

The occurrence of phlogopite phenocrysts (Table 2), amphibole xenocrysts and mantle xenoliths containing phlogopite in the mafic K-rich magmatic rocks of south Tibet (e.g., Miller et al. 1999; Williams et al. 2001; Zhao et al. 2008, 2009; Liu et al. 2011) indicates hydrous melting of the mantle source (Bizimis et al. 2000). Under hydrous melting conditions, the melting mineral mode of the MORB-source mantle is clinopyroxene (0.56), olivine ( $-0.10$ ), orthopyroxene (0.52) and spinel (0.02) (Bizimis et al. 2000). Because additional mineral phases (e.g., phlogopite, amphibole and apatite) are formed during mantle metasomatism, and phlogopite, amphibole, apatite, spinel and clinopyroxene are considered to be completely consumed into the melt before olivine and orthopyroxene, based on the previous studies, we assumed the following mineral melting mode (i.e., the proportion of the mineral phases entering the melt, following Guo et al. 2005, 2006): apatite (0.015), clinopyroxene (0.55), olivine ( $-0.10$ ), orthopyroxene (0.40), phlogopite (0.03), amphibole (0.032), rutile (0.003), titanite (0.05) and spinel (0.02). The mineral–melt partition coefficients for the trace elements in the residual mineral phases used in the model (Table 7) are based on those from the GERM Web site (<http://www.earthref.org>).

On the basis of our estimates of the mixing proportions of the three end-member components (fluid, melt and MORB-source mantle wedge) in the mantle source of the XDY rift magmas (Fig. 11), we calculated the trace element concentrations in the mixed mantle source (Table 8), following the calculation method of Elburg et al. (2002) and Guo and Wilson (2012). As noted earlier, we selected a biotite paragneiss to represent the bulk HHCS composition in the trace element modeling because it is thought to be more easily melted with respect to other lithologies in the HHCS (Richards et al. 2005; Guo and Wilson 2012). Based

**Table 7** Mineral–melt partition coefficients for trace element model calculations

	Am	Phl	Ap	Cpx	Opx	Ol	Rut	Tit	Sp
Rb	0.58	5.18	0.4	0.0047	0.02	0.04	0.0076		
Ba	6.4	3.48	0.05	0.00061	0.03	5.45E–06	0.0137	0.6	
Th	0.054	0.0145	17.1	0.0127	0.0000225	0.0000062	0.54		
U	0.05	0.26	1.82	0.145	0.028	0.01			
Nb	0.127	0.0853		0.0027	0.105	0.063	13.1	4.6	0.085
Ta	0.56	0.1069	0.05	0.19	0.159	0.01	5	14.85	0.08
K	2.3	8.87		0.0135	0.0003	0.04			
La	0.54	0.0322	3.7	0.031	0.00045	0.0004	0.0055	5.35	0.01
Ce	0.055	0.0078	11.2	0.0843	0.0011	0.1	0.087		0.01
Pb	0.6	0.04	0.03	0.014	0.0013	0.000274			
Sr	0.33	0.183	1.2	0.512	0.09	0.0000331	0.036		
P			20	0.03	0.03	0.055	0.05		
Nd	0.17	0.08	14	0.173	0.0039	0.0096	0.277		0.01
Sm	0.535	0.0365	4.5	0.312	0.01095	0.0013	0.00164		0.01
Zr	0.33	0.0232	0.636	0.195	0.22	0.12	3.07		0.085
Hf	0.43	0.19	0.4	0.2	0.6	0.02	4.98		0.055
Eu	2.88	0.05	23.8	0.336	0.01	0.0016	0.00037	0.135	0.01
Ti	3.06			0.89	0.024	0.007	11	35.7	0.048
Tb	2	0.35	3.49	0.408	2.6	0.1			0.01
Y	0.298	0.007	162	0.438	1.1	0.072	0.076		
Yb	0.51	0.0484	8.1	0.265	0.097	0.2685	0.0093	104	0.01
Lu	0.4	0.2	3.8	0.439	0.098	0.0694	0.0124	92	0.01

Blank denotes no data are available

Data sources of mineral–melt partition coefficients: GERM (Geochemical Earth Reference Model) home page, <http://www.earthref.org/>

The solid (HHCS)–fluid partition coefficients (Johnson and Plank 1999) as follows: 2.00 (Rb); 0.84 (Ba); 4.81 (Th); 1.37 (U); 2.65 (Nb); 2.00 (Ta); 2.61 (K); 4.00 (La); 4.01 (Ce); Pb (0.64); 0.53 (Sr); 2.53 (P); 3.26 (Nd); 2.41 (Sm); 2.3 (Zr); 2.00 (Hf); 2.27 (Eu); 2.21 (Ti); 1.52 (Tb); 1.16 (Y); 1.06 (Yb); 1.05 (Lu)

Am amphibole, Ap apatite, Cpx clinopyroxene, Ol olivine, Opx orthopyroxene, Phl phlogopite, Rut rutile, Tit titanite, Sp spinel

on the above data (i.e., residual mineral assemblages, mineral–melt partition coefficients, melting mineral mode and trace element contents in the enriched mantle source), we quantitatively simulated the trace element contents in the XDY rift magmas using an iterative calculation technique, based on the approach of Guo et al. (2005, 2006). The outline of the iterative calculation procedure is as follows. First, we selected two initial parameters in the model partial melting equations (Wilson 1989); these are (1) the partial melting degree and (2) the residual mineral proportions in the mantle source. Second, we selected a potential range for the melting degree from 0 to 80 % with calculated step of 1 % based on the previously published results for the melting degree required for K-rich magma generation (Williams et al. 2004; Guo et al. 2005, 2006). Additionally, considering the likely presence of new mineral phases in the source (e.g., phlogopite, amphibole and apatite) formed during metasomatism of the mantle wedge, we assumed that the resultant mineral modes (and their potential ranges) in the enriched mantle caused by addition

of the subduction-derived fluid and melt were as follows: olivine (from 10 to 80 %), orthopyroxene (from 5 to 60 %), clinopyroxene (from 5 to 60 %), spinel (from 0 to 10 %), phlogopite (from 0 to 20 %), amphibole (from 0 to 20 %), rutile (from 0 to 20 %), titanite (from 0 to 20 %) and apatite (from 0 to 10 %), based on the previous melting experiments and model simulations (e.g., Bizimis et al. 2000; Melzer and Foley 2000; Williams et al. 2004; Guo et al. 2005, 2006; Holbig and Grove 2008). Third, on the basis of the above ranges in the initial parameters, we carried out iterative model melting calculations by changing the parameters from the minimum to maximum values within their respective potential ranges. When the calculation results of the model simulations provided the best fit to the actual trace element concentrations in the XDY rift primitive mafic magmatic rocks, we terminated the iteration and recorded the final values of the trace element content, residual mineral proportions and melting degree of the mantle source (Fig. 14). Thus, the final calculation results of the trace element melting model give the best-fit

**Table 8** The best-fit results of the trace element modeling

Field name	Garwa	Yaqian	Mibale	Chazi
Melting degree	$F = 1 \%$	$F = 2 \%$	$F = 8 \%$	$F = 10 \%$
Fluid in source (in average)	0 %	0 %	0.5 %	3.0 %
Melt in source (in average)	2.0 %	3.0 %	5.0 %	8.0 %
Rb	1,378.16	601.49	865.35	942.89
Ba	5,273.25	3,420.14	5,069.41	5,210.81
Th	380.59	237.81	290.52	369.73
U	34.54	25.94	26.37	39.79
Nb	35.46	33.22	46.95	67.86
Ta	1.79	1.67	2.64	4.22
K	205,943	82,763	133,947	125,800
La	281.53	234.30	299.53	425.38
Ce	645.44	485.63	579.29	797.74
Pb	154.58	99.31	67.03	151.42
Sr	913.68	815.46	798.87	1,019.37
P	5,450	3,755	3,695	4,092
Nd	170.77	117.85	131.51	165.24
Sm	50.56	40.15	36.36	43.33
Zr	627.21	601.13	712.56	1,020.43
Hf	20.58	19.86	30.68	50.53
Eu	6.50	4.75	4.88	4.79
Ti	9,189	8,624	9,719	10,314
Tb	1.11	1.10	1.72	2.99
Y	29.52	21.63	24.16	24.11
Yb	1.89	1.75	2.02	2.45
Lu	0.34	0.32	0.37	0.44

Contents of the elements are in ppm. Field name corresponds to that in Fig. 1

For more detailed discussions for the trace element model calculation, see the main text

The trace element concentrations in the fluid and melt derived from the HHCS are calculated following the method described in Table 6. The expression and approach of the non-modal batch partial melting model follow those of Guo et al. (2005, 2006, 2007)

values of the degree of melting of the mantle source and the residual mineral proportions in the mantle source during the formation of the XDY rift magmas (Fig. 14; Table 8). Details of the iterative calculation method for the trace element modeling are given in Guo et al. (2005, 2006, 2007) and Guo and Wilson (2012).

The best-fit model results indicate that a melt with trace element characteristics similar to those of the K-rich rocks could be generated by 8–10 % partial melting of a metasomatized mantle source in the south and 1–2 % melting in the north of the XDY rift. The residue has relatively high proportions of apatite (0.9–1.2 %), phlogopite (1.6–3.2 %) and amphibole (1.2–3 %) in the south, but a lower amount of apatite (0.5 %), phlogopite (0.5 %) and amphibole (1.0 %) in the north of the rift (Table 8; Fig. 14). The calculation results indicate that the degree of partial melting of the mantle source region decreases from south to north (Figs. 1, 14). This is consistent with the higher LILE contents and steeper LREE patterns of the K-rich magmatic

rocks in the north compared to those in the south of the XDY rift (Figs. 5, 6).

As in any modeling calculations, there are sources of error whose effects on the modeling results must be assessed. We quantified the relative errors on the trace element modeling by the comparison between the analytical results and the modeled values of the trace element concentrations (Fig. 14) and by factor analysis of the potential sources of error in the trace element modeling calculations. The sources of error in the trace element modeling can be attributed to the selections of the initial parameters (e.g., MORB-source mantle composition, partition coefficients and the melting proportions of the mineral phases). However, sensitivity analyses and calculations indicate that the effect of relative changes in the initial parameters on the final results of the trace element modeling is not significant; this is about 1–5 % for the trace elements shown in Fig. 14. The variation trends in Fig. 14 are similar even when the initial parameters are changed significantly.

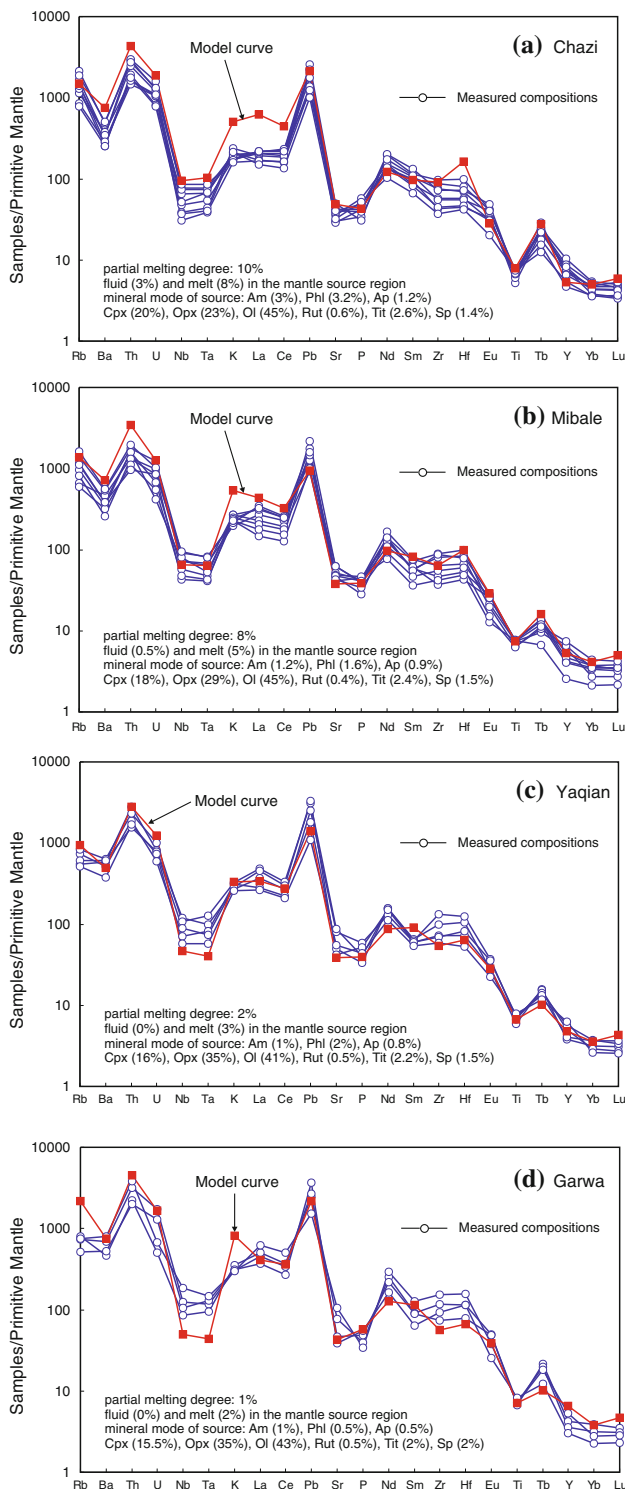


**Fig. 14** Comparison between the observed compositions of the K-rich magmatic rocks (electronic supplementary material 1) and our trace element model curves, simulated by a non-modal batch melting model. **a** Chazi; **b** Mibale; **c** Yaqian; **d** Garwa. The detailed calculation procedures are explained in the text, Tables 7 and 8. *Am* amphibole, *Ap* apatite, *Cpx* clinopyroxene, *Ol* olivine, *Opx* orthopyroxene, *Phl* phlogopite, *Rut* rutile, *Tit* titanite, *Sp* spinel

## A geodynamic model for the petrogenesis of post-collisional, K-rich rocks in south Tibet

Previous studies have ascribed the petrogenesis of the post-collisional, potassium-rich magmatic rocks in south Tibet to convective thinning of the subcontinental lithospheric mantle (e.g., Williams et al. 2001, 2004; Chung et al. 2003) or to break-off of the subducted Indian continental lithosphere slab (e.g., Kohn and Parkinson 2002; Maheo et al. 2002). The narrow, near east–west striking belt of post-collisional, K-rich magmatic rocks in south Tibet (Fig. 1a) cannot easily be explained by decompression melting induced by delamination of previously thickened lithosphere (Guo et al. 2007) because this would be unlikely to occur along such a narrow, linear zone. Moreover, a model of convective thinning of the subcontinental lithospheric mantle can hardly explain the decreasing trend in the age of the magmatism from north to south (Fig. 2) or the across-arc trends in the proportions of the metasomatic components in the mantle source (Figs. 7, 11). Additionally, seismic tomographic studies (e.g., Zhou and Murphy 2005; Li et al. 2008; Zhao et al. 2010, 2011) have indicated the continuous presence of a northward dipping subducted slab of Indian continental lithosphere which increases in depth from south to north beneath south Tibet, precluding the hypothesis of subducted Indian slab break-off at 25 Ma. If slab break-off did occur and the post-collisional magmas in south Tibet did result from such a process, then we need to ask why the post-collisional, K-rich magmatism only occurred between 25 and 8 Ma and why no magmas were derived from subslab asthenospheric (MORB or OIB source) mantle which would have risen through the resultant slab window.

The ages (25–8 Ma) of the post-collisional, K-rich magmatic rocks in south Tibet clearly postdate by some 30 Myr the India–Asia collision at 55 Ma; this delay suggests that the petrogenesis of the K-rich magmas cannot be directly explained by the northward subduction of the Indian lithospheric slab. However, the proportion of enriched components (fluids and melts), derived from the subducted HHCS, in the metasomatized mantle source of the magmatic rocks decreases from south to north along the XDY rift, indicating that the enrichment of the mantle source was induced by continued northward subduction of Indian continental lithosphere following the India–Asia collision at ~55 Ma. Among the most important questions remaining is why the post-collisional, K-rich magmatism only occurred between 25 and 8 Ma in south Tibet.

The post-collisional, K-rich magmatic rocks in the XDY rift have relatively high MgO contents, Mg numbers and Ni contents (electronic supplementary material 1), indicating

that they are partial melting products of the upper mantle. The age (23–8 Ma) of the magmatism (Table 1) is consistent with the age range (25–8 Ma) of the post-collisional magmatism in the other volcanic fields within south Tibet (e.g., Miller et al. 1999; Ding et al. 2003; Gao et al. 2007; Zhao et al. 2009; Chen et al. 2010, 2012). This signals an important tectono-magmatic event which may have led to the partial melting of the upper mantle around 30 Myr after India–Asia collision at  $\sim 55$  Ma. This event could have involved the addition of metasomatizing fluids and/or melts to the mantle source region, heating and/or decompression (Wilson 1989). However, there is little geophysical evidence to support overheating melting of the upper mantle during the period 25–8 Ma because of the northward underthrusting of the Indian continental lithospheric mantle beneath the southern Tibetan Plateau (e.g., Nelson et al. 1996; Zhou and Murphy 2005; Li et al. 2008; Zhao et al. 2011). The decreasing amounts of the subducted HHCS-derived fluid and melt components in the mantle source region from south (front-arc) to north (rear-arc) in south Tibet can be easily explained by continued northward underthrusting of the Indian continental lithosphere following India–Asia collision at  $\sim 55$  Ma (Figs. 11, 15a). The increasing age of the XDY rift K-rich magmatic rocks from south to north (Table 1; Fig. 2) indicates that melting of the metasomatized mantle source region is not well explained by the northward underthrusting of Indian lithosphere, although it could contribute to the three-component (fluid, melt and MORB-source mantle wedge) mixing in the mantle source region. If melting of the metasomatized mantle source were directly triggered by the progressive northward underthrusting of the Indian continental lithosphere, it would generate progressively decreasing ages for the resultant K-rich magmatic rocks from south to north within the XDY rift (Fig. 1), rather than decreasing ages from north to south as shown in Fig. 2. Moreover, the age of onset of the K-rich magmatism would be same as that of the northward underthrusting of the Indian continental lithosphere at  $\sim 55$  Ma, rather than 30 Myr after India–Asia collision (Table 1; Fig. 2). Thus, the mantle melting responsible for generation of the K-rich magmas cannot simply be attributed to the addition of subduction-related metasomatic components (fluids and melts) to the mantle source region. The addition of such components instead mainly resulted in the enrichment of the mantle source. Consequently, decompression is the only process that could have triggered the melting of the enriched mantle source. The following observations provide supporting evidence for decompression melting between 25 and 8 Ma in south Tibet. (1) Our detailed field observations, combined with the results from previous studies (Williams et al. 2001; Hou et al. 2004; Gao et al. 2007; Zhao et al. 2009), indicate a close correlation between the

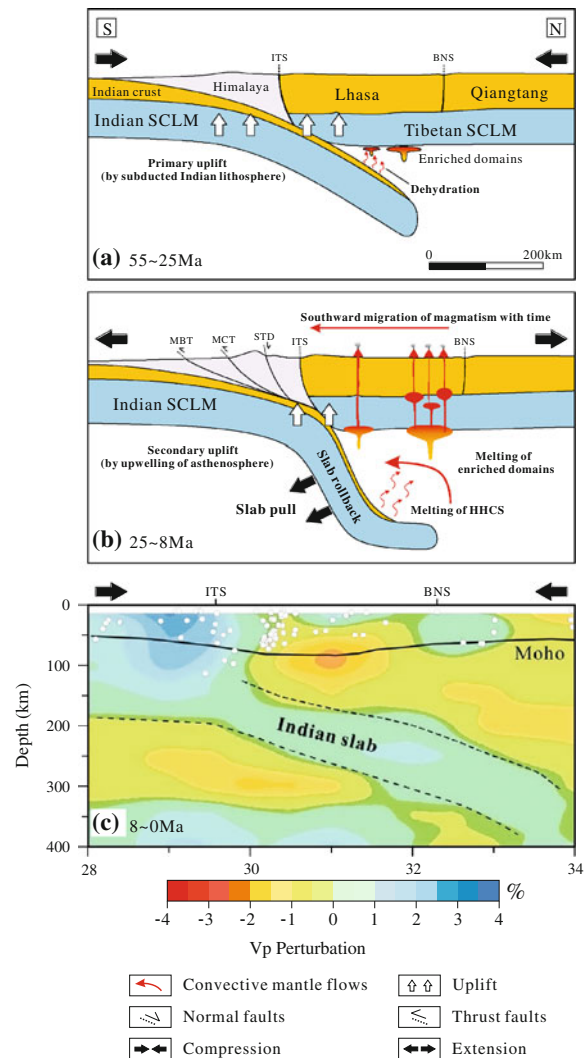


**Fig. 15** Petrogenetic model for the post-collisional, K-rich magmatism in south Tibet. The diagram shows a N–S cross section. **a** Northward underthrusting of the HHCS (Indian crust) beneath the Lhasa terrane caused compressional deformation in south Tibet and the Himalayas from 55 to 25 Ma. The northward subduction led to the generation of fluid-metasomatized domains in the mantle wedge resulting from enrichment by addition of fluids derived from dehydration of the subducted HHCS. **b** The mantle wedge was further enriched by mixing of the fluid-metasomatized domains with a partial melt of the already dehydrated HHCS, forming regions of low melting-point metasomatized mantle. These undergo decompressional partial melting because of slab rollback and upwelling of asthenospheric mantle, resulting in the generation of the post-collisional, K-rich magmatism in an extensional tectonic setting. **c** Teleseismic tomographic image showing the presence of the northward underthrusting Indian slab and the low-velocity area beneath south Tibet at the present day. White dots show the locations of earthquakes ( $M > 4.5$ ) that occurred within 30 km of the profile (He et al. 2010). This diagram is based on the studies of Kosarev et al. (1999), Tilmann et al. (2003), Li et al. (2008), He et al. (2010) and Guo and Wilson (2012). BNS Bangong–Nujiang suture, ITS Indus–Tsangpo suture, MBT the Main Boundary thrust, MCT the Main Central thrust, STD south Tibetan detachment, N north, S south, SCLM subcontinental lithospheric mantle. Red-filled triangles represent the locations of post-collisional, potassium-rich magmatism in south Tibet

outcrops of the post-collisional, K-rich magmatic rocks and a series of N–S-trending rifts in south Tibet (Fig. 1). The orientation of the rifts has been ascribed to east–west extension during the period 25–8 Ma (Williams et al. 2001; Guo et al. 2007). The preceding phase of Linzizong volcanism from 65 to 40 Ma forms a continuous E–W-trending magmatic belt in south Tibet (Fig. 1a); this is clearly different from the distribution of N–S striking, post-collisional, K-rich magmatism from 25 to 8 Ma (Fig. 1b). The change in the trend of the distribution of the volcanic rocks signals the onset of extension in south Tibet at ~25 Ma. (2) Lee and Lawver (1995) suggested that the India–Asia convergence rate decreased between 25 and 8 Ma. This could have led directly to extension as a consequence of rollback of the subducted Indian slab beneath south Tibet. This observation is consistent with lithospheric flexural bending and steepening of the northward subducting Indian slab since the early Miocene (e.g., Replumaz et al. 2004; King et al. 2011). (3) Recent studies (e.g., Zhang et al. 2010, 2011; Husson et al. 2012) have indicated that slab rollback can lead to a younging trend in igneous activity from the rear-arc to the front-arc because of decompression melting and upwelling of the asthenosphere. The southward decreasing trend in the ages of the K-rich magmatic rocks (Table 1; Fig. 2) is consistent with the rollback of the northward subducted Indian slab between 25 and 8 Ma. Such a slab rollback model also can result in re-heating of the mantle beneath south Tibet, caused by upwelling of the asthenospheric mantle which could have triggered mantle melting. This suggests that slab rollback not only caused the extensional tectonics but also led to an increase in the temperature and depth of the top of the subducted slab between 25 and 8 Ma. (4) Previous studies (e.g., Class et al. 2000; Elburg et al. 2002) have indicated a change in slab-to-wedge transport from a fluid to a partial melt with increasing temperature and depth to the top of the subducting slab, consistent with a slab rollback model.

Our Sr–Nd–Pb isotopic and trace element data are best explained by melting of a MORB-source mantle wedge sequentially metasomatized by fluids then melts (Figs. 11, 14), indicating that the HHCS-derived fluids were first transported into the overlying MORB-source mantle wedge at shallow depths and then dehydrated HHCS underwent melting at greater depths and higher temperature conditions, producing the partial melts that further enriched the subarc mantle. This model suggests that the subducted HHCS first dehydrated as a consequence of the northward underthrusting of the Indian continental lithosphere, forming hydrous fluids at shallow mantle depths during the period 55 to 25 Ma (Fig. 15a); subsequently, the dehydrated HHCS ultimately melted in response to slab rollback-induced temperature increases between 25 and 8 Ma (Fig. 15b). The increase in the amount of subducted slab-derived melts transported into the overlying mantle wedge

from the rear-arc (north) to front-arc (south) indicates higher temperatures and greater depths to the top of the slab in the south than in the north of the XDY rift, suggesting slab southward pull, downward bending and then southward suction of hot asthenospheric mantle into the mantle wedge between 25 and 8 Ma (Fig. 15b). This is consistent with an extensional tectonic regime during this period (Fig. 15b). Consequently, the first-stage mixing between MORB-source mantle wedge and a fluid derived from subducted HHCS in the mantle source of the magmas occurred during the period 55–25 Ma, whereas the second-stage mixing between the fluid-modified mantle wedge and a partial melt from dehydrated HHCS mainly occurred during the period 25–8 Ma.

The preceding phase of subduction-related Linzizong volcanism lasted from 65 to 40 Ma (Mo et al. 2008). There are no occurrences of post-collisional, K-rich magmatism between 40 and 25 Ma in south Tibet, leading to a “magmatic gap” lasting for some 15 Myr (Maheo et al. 2002; Chung et al. 2005; Gao et al. 2007; Mo et al. 2007; Xu et al. 2008). This “magmatic gap” can be explained by reduced enrichment of the mantle source during this period. The fluid enrichment during stage 1 was not sufficient to cause partial melting of the two-component (MORB-source mantle plus fluid) mixed mantle source, perhaps because the metasomatism was too weak, the mantle wedge was too cold and also under strong compression during the northward subduction of the Indian slab between 55 and 25 Ma (Fig. 15a). Stage 1, however, contributed to primary uplift in south Tibet because of the strong northward underthrusting of the Indian continental lithosphere from 55 to 25 Ma (Fig. 15a). The occurrence of the post-collisional, K-rich magmatism during stage 2 signals an important extension-induced decompression melting event caused by slab rollback as a consequence of the decreasing convergence rate between India and Asia from 25 to 8 Ma (Fig. 15b). There may have been secondary uplift in south Tibet during this period caused by upwelling of hot asthenospheric mantle and lithospheric flexure, as suggested by Guo and Wilson (2012). This is consistent with the spatial correlation between the post-collisional, K-rich magmatism and the N–S-trending rifts in south Tibet (Fig. 1). The K-rich magmatic rocks are older than 8 Ma (Table 1), indicating cessation of extension and slab rollback by 8 Ma. This is supported by significant uplift of the south Tibet–Himalaya orogen since ca. 7 Ma (Wang et al. 2006), suggesting renewed compression. Thus, there has been no post-collisional, K-rich magmatism in south Tibet since 8 Ma because there has been less enrichment of the mantle wedge than previously, driven only by the addition of fluids derived from the subducted Indian lithosphere (Fig. 14c). This is similar to the earlier scenario from 55 to 25 Ma in south Tibet (Fig. 15a).

## Lithospheric mantle versus asthenospheric mantle source region of the K-rich magmas

Previous studies (e.g., Ding et al. 2003; Chung et al. 2005) suggested that the source region of the K-rich magmas in south Tibet is enriched lithospheric mantle. In contrast, our Sr–Nd–Pb isotopic and trace element modeling simulations (Figs. 11, 14) indicate that source region of the K-rich magmas is an asthenospheric mantle wedge enriched by the addition of HHCS-derived fluids and melts. The linear trends between MORB and HHCS in the Sr–Nd–Pb isotope diagrams support this inference (Fig. 8). The Ta–Nb–Ti depletions in mantle-normalized trace element diagrams (Fig. 6), together with the east–west linear distribution of the K-rich magmatic rocks to the north of the ITS (Fig. 1a) show that the enrichment of the asthenospheric mantle wedge resulted from northward subduction of the Indian slab since the India–Asia collision at 55 Ma. Many recent seismic tomographic studies also indicate the presence of a northward subducting Indian slab beneath south Tibet (e.g., Zhao et al. 2010, 2011). Southward rollback of the subducted Indian slab during the period 25–8 Ma resulted in the observed decreases in the age of the magmatism (Fig. 2), the linear trends in Sr–Nd–Pb isotopic and trace element ratios (Fig. 7) and enriched component (fluid and melt) increases in the source of the magmas (Fig. 11) from north to south in the XDY rift. In contrast, these spatial, temporal and compositional variations of the K-rich magmas from north to south cannot easily be explained by melting of an enriched lithospheric mantle source because the age and compositional trends (Figs. 2, 7, 11) cannot form in the lithospheric mantle of the upper plate. Previous studies (e.g., Kincaid and Sacks 1997; Kincaid and Griffiths 2004) have indicated that subduction of cold, thick continental lithosphere can cause low temperatures in the supra-subduction zone mantle wedge and therefore lead to the stabilization of hydrous mineral phases (e.g., amphibole, phlogopite) in the mantle wedge, forming enriched domains. The rollback of the subducted Indian slab, accompanied by suction of hot asthenospheric mantle, led to melting of these hydrous phases in the enriched domains of the mantle wedge during the period 25–8 Ma, forming the post-collisional, K-rich mafic magmas.

## Conclusions

Based on bulk-rock major and trace element and Sr–Nd–Pb isotopic data, combined with geochronological data, we propose a two-stage model to explain the petrogenesis of the post-collisional, mafic K-rich magmatism of south Tibet. Stage 1 contributed fluids to a depleted mantle wedge to form a two-component mixed mantle source by

the northward underthrusting of Indian continental lithosphere from ~55 to 25 Ma. Stage 2 led to further enrichment of the mantle source by addition of partial melts derived from the previously dehydrated Indian slab in response to slab rollback and finally resulted in the decompression melting of the enriched, three-component, mantle source to form the post-collisional, K-rich magmas in south Tibet between 25 and 8 Ma. Continental subduction-induced uplift may have occurred during stage 1 in south Tibet because of the northward underthrusting of the Indian continental lithosphere producing a strongly compressive stress regime. The post-collisional, K-rich magmatism in south Tibet may signal an important change to extension-induced mantle melting as a consequence of the decreasing convergence rate between India and Asia from 25 to 8 Ma. Uplift of south Tibet during this period may have occurred because of the flexural bending of the subducted lithosphere and asthenospheric upwelling. Three factors (including the degree of partial melting, the proportion of residual minerals and the amount of subduction-derived components (fluid or melt) in the mantle source) provide important drivers for the change in the composition of the post-collisional, mafic K-rich magmas from south (front-arc) to north (rear-arc) within the XDY rift. The increases in the abundances of some incompatible elements from south to north can be explained by decreasing degrees of partial melting and gradual changes in the proportions of the residual minerals in the mantle source, whereas the across-arc trends in Sr–Nd–Pb isotopic and trace element ratios can be attributed to a decrease in the amount of subduction-derived components (fluids and melts) added to the MORB-source mantle wedge from the front-arc (south) to the rear-arc (north). Our study indicates that the post-collisional, mafic K-rich magmatism in south Tibet can provide an effective petrologic indicator of slab rollback-induced extension in the Himalayan–Tibetan orogen between 25 and 8 Ma.

**Acknowledgments** This study was supported by a special project grant from the Chinese Academy of Sciences (XDB03010600), grants from National Natural Science Foundation of China (NSFC) (No: 41020124002 and 41130314) and a joint project between the Royal Society of London and NSFC. We thank Drs Y. Shi and Y. Di for assistance with zircon age measurements. We are grateful to J. Liu, X. Chen, X. Li and W. Guo for their assistance. The referees (Sebastian Tappe and Jörg Pfänder) are acknowledged for their extremely constructive reviews of an earlier version of the manuscript. We also thank the editor, Hans Keppler, for his support.

## References

- Ahmad T, Harris N, Bickle M, Chapman H, Bunbury J, Prince C (2000) Isotopic constraints on the structural relationships between the lesser Himalayan series and the high Himalayan crystalline series, Garhwal Himalaya. *Geol Soc Am Bull* 112:467–477

- Ali JR, Aitchison JC (2008) Gondwana to Asia: plate tectonics, paleogeography and the biological connectivity of the Indian sub-continent from the middle Jurassic through latest Eocene (166–35 Ma). *Earth Sci Rev* 88:145–166
- Altherr R, Meyer HP, Holl A, Volker F, Alibert C, McCulloch MT, Majer V (2004) Geochemical and Sr-Nd-Pb isotopic characteristics of Late Cenozoic leucite lamproites from the East European Alpine belt (Macedonia and Yugoslavia). *Contrib Mineral Petrol* 147(1):58–73
- Arnaud NO, Vidal P, Tapponnier P, Matte P, Deng WM (1992) The high K<sub>2</sub>O volcanism of northwestern Tibet: geochemistry and tectonic implications. *Earth Planet Sci Lett* 111:351–367
- Benito R, López-Ruiz J, Cebriá JM, Hertogen J, Doblas M, Oyarzun R, Demaiffe D (1999) Sr and O isotope constraints on source and crustal contamination in the high-K calc-alkaline and shoshonitic Neogene volcanic rocks of SE Spain. *Lithos* 46:773–802
- Bizimis M, Salters VJM, Bonatti E (2000) Trace and REE content of clinopyroxenes from supra-subduction zone peridotites. Implications for melting and enrichment processes in island arcs. *Chem Geol* 165:67–85
- Black LP, Kamo SL, Allen CM, Aleinikoff JN, Davis DW, Korsch RJ, Foudoulis C (2003a) TEMORA 1: a new zircon standard for Phanerozoic U-Pb geochronology. *Chem Geol* 200:155–170
- Black LP, Kamo SL, Williams IS, Mundil R, Davis DW, Korsch RJ, Foudoulis C (2003b) The application of SHRIMP to Phanerozoic geochronology; a critical appraisal of four zircon standards. *Chem Geol* 200:171–188
- Black LP, Kamo SL, Allen CM, Davis DW, Aleinikoff JN, Valley JW, Mundil R, Campbell IH, Korsch RJ, Williams IS, Foudoulis C (2004) Improved <sup>206</sup>Pb/<sup>238</sup>U microprobe geochronology by the monitoring of a trace-element-related matrix effect; SHRIMP, ID-TIMS, ELA-ICP-MS and oxygen isotope documentation for a series of zircon standards. *Chem Geol* 205:115–140
- Blisniuk PM, Hacker BR, Glodny J, Ratschbacher L, Bi S, Wu Z, McWilliams MO, Calvert A (2001) Normal faulting in central Tibet since at least 13.5 Myr ago. *Nature* 412:628–632
- Boari E, Avanzinelli R, Melluso L, Giordano G, Mattei M, De Benedetti AA, Morra V, Conticelli S (2009) Isotope geochemistry (Sr–Nd–Pb) and petrogenesis of leucite-bearing volcanic rocks from “Colli Albani” volcano, Roman Magmatic Province, Central Italy: inferences on volcano evolution and magma genesis. *Bull Volcanol* 71:977–1005
- Cai F, Ding L, Yue Y (2011) Provenance analysis of upper Cretaceous strata in the Tethys Himalaya, southern Tibet: implications for timing of India-Asia collision. *Earth Planet Sci Lett* 305:195–206
- Chen JL, Xu JF, Kang ZQ, Wang BD (2007) Geochemistry and origin of Miocene volcanic rocks in Caze area, south-western Qinghai-Xizang plateau. *Geochimica* 36:457–466 (in Chinese with English abstract)
- Chen JL, Xu JF, Kang ZQ, Wang BD (2008) Geochemical comparison of the Cenozoic high-MgO-potassic volcanic rocks between northern and southern of Tibetan plateau: difference of the both mantle sources. *Acta Petrol Sin* 24:211–224 (in Chinese with English abstract)
- Chen JL, Xu JF, Wang BD, Kang ZQ, Li J (2010) Origin of Cenozoic alkaline potassic volcanic rocks at KonglongXiang, Lhasa terrane, Tibetan Plateau: products of partial melting of a mafic lower-crustal source? *Chem Geol* 273:286–299
- Chen JL, Xu JF, Zhao WX, Dong YH, Wang BD, Kang ZQ (2011) Geochemical variations in Miocene adakitic rocks from the western and eastern Lhasa terrane: implications for lower crustal flow beneath the southern Tibetan plateau. *Lithos* 125:928–939
- Chen JL, Zhao WX, Xu JF, Wang BD, Kang ZQ (2012) Geochemistry of Miocene trachytes in Bugasi, Lhasa block, Tibetan plateau: mixing products between mantle-and crust-derived melts? *Gondwana Res* 21:112–122
- Chung SL, Lo CH, Lee TY, Zhang Y, Xie Y, Li X, Wang KL, Wang PL (1998) Diachronous uplift of the Tibetan plateau starting 40 Myr ago. *Nature* 394:769–773
- Chung SL, Liu D, Ji J, Chu MF, Lee HY, Wen DJ, Lo CH, Lee TY, Qian Q, Zhang Q (2003) Adakites from continental collision zones: melting of thickened lower crust beneath southern Tibet. *Geology* 31:1021–1024
- Chung SL, Chu MF, Zhang Y, Xie Y, Lo CH, Lee TY, Lan CY, Li X, Zhang Q, Wang Y (2005) Tibetan tectonic evolution inferred from spatial and temporal variations in post-collisional magmatism. *Earth Sci Rev* 68:173–196
- Class C, Miller DM, Goldstein SL, Langmuir CH (2000) Distinguishing melt and fluid subduction components in Umnak volcanics, Aleutian arc. *Geochem Geophys Geosyst* 1. doi:10.1029/1999GC000010
- Conticelli S, Peccerillo A (1992) Petrology and geochemistry of potassic and ultrapotassic volcanism in central Italy: petrogenesis and inferences on the evolution of the mantle sources. *Lithos* 28:221–240
- Conticelli S, Guarnieri L, Farinelli A, Mattei M, Avanzinelli R, Bianchini G, Boari E, Tommasini S, Tiepolo M, Prelević D, Venturelli G (2009) Trace elements and Sr–Nd–Pb isotopes of K-rich, shoshonitic, and calc-alkaline magmatism of the western Mediterranean region: genesis of ultrapotassic to calc-alkaline magmatic associations in a post-collisional geodynamic setting. *Lithos* 107:68–92
- Contini S, Venturelli G, Toscani L, Capedri S, Barbieri M (1993) Cr–Zr-arnalcolite-bearing lamproites of Cancarix, SE Spain. *Mineral Mag* 57(387):203–216
- Coulon C, Maluski H, Bollinger C, Wang S (1986) Mesozoic and Cenozoic volcanic rocks from central and southern Tibet: <sup>39</sup>Ar–<sup>40</sup>Ar dating, petrological characteristics and geodynamical significance. *Earth Planet Sci Lett* 79:281–302
- DeCelles PG, Robinson DM, Zandt G (2002) Implications of shortening in the Himalayan fold-thrust belt for uplift of the Tibetan plateau. *Tectonics* 21:1062. doi:10.1029/2001TC001322
- Deng JF, Mo XX, Zhao HL, Wu ZX, Luo ZH, Su SG (2004) A new model for the dynamic evolution of Chinese lithosphere: ‘continental roots-plume tectonics’. *Earth Sci Rev* 65:223–275
- DePaolo DJ (1988) Neodymium isotope geochemistry: an introduction. Springer, New York
- Ding L, Kapp P, Zhong D, Deng W (2003) Cenozoic volcanism in Tibet: evidence for a transition from oceanic to continental subduction. *J Petrol* 44:1833–1865
- Ding L, Kapp P, Wan X (2005) Paleocene-Eocene record of ophiolite obduction and initial India-Asia collision, south central Tibet. *Tectonics* 24:TC3001. doi:10.1029/2004TC001729
- Ding L, Yue Y, Cai F, Xu X, Zhan Q, Lai Q (2006) <sup>40</sup>Ar/<sup>39</sup>Ar geochronology, geochemical and Sr–Nd–O isotopic characteristics of the high-Mg ultrapotassic rocks in Lhasa block of Tibet: implications in the onset time and depth of NS-striking rift system. *Acta Geol Sinica* 80:1252–1261 (in Chinese with English abstract)
- Elburg MA, Bergen MA, Hoogewerff J, Foden J, Vroon P, Zulkarnain I, Nasution A (2002) Geochemical trends across an arc-continent collision zone: magma sources and slab-wedge transfer processes below the Pantar Strait volcanoes, Indonesia. *Geochim Cosmochim Acta* 66:2771–2789
- Faure G, Mensing TM (2005) Isotopes: principles and applications. John Wiley & Sons, New Jersey, pp 1–897
- Foley SF, Venturelli G, Green DH, Toscani L (1987) The ultrapotassic rocks: characteristics, classification, and constraints for petrogenetic models. *Earth Sci Rev* 24:81–134
- Furman T, Graham D (1999) Erosion of lithospheric mantle beneath the East African Rift system: geochemical evidence from the Kivu volcanic province. *Lithos* 48:237–262

- Gao Y, Hou Z, Kamber BS, Wei R, Meng X, Zhao R (2007) Lamproitic rocks from a continental collision zone: evidence for recycling of subducted Tethyan oceanic sediments in the mantle beneath southern Tibet. *J Petrol* 48:729–752
- Gasperini D, Blichert-Toft J, Bosch D, Del Moro A, Macera P, Albarède F (2002) Upwelling of deep mantle material through a plate window: evidence from the geochemistry of Italian basaltic volcanics. *J Geophys Res* 107:2367
- GERM website: <http://www.earthref.org/>
- Gill JB (1981) Orogenic andesites and plate tectonics. Springer, Berlin, pp 1–390
- Goldstein SL, O’Nions RK, Hamilton PJ (1984) A Sm-Nd isotopic study of atmospheric dusts and particulates from major river systems. *Earth Planet Sci Lett* 70:221–236
- Govindaraju K (1994) Compilation of working values and sample description for 383 geostandards. *Geostand Newslett* 18(special issue):1–158
- Guo Z, Wilson M (2012) The Himalayan leucogranites: constraints on the nature of their crustal source region and geodynamic setting. *Gondwana Res* 22:360–376
- Guo Z, Hertogen J, Liu J, Pasteris P, Boven A, Punzalan L, He H, Luo X, Zhang W (2005) Potassic magmatism in western Sichuan and Yunnan provinces, SE Tibet, China: petrological and geochemical constraints on petrogenesis. *J Petrol* 46:33–78
- Guo Z, Wilson M, Liu J, Mao Q (2006) Post-collisional, potassic and ultrapotassic magmatism of the northern Tibetan plateau: constraints on characteristics of the mantle source, geodynamic setting and uplift mechanisms. *J Petrol* 47:1177–1220
- Guo Z, Wilson M, Liu J (2007) Post-collisional adakites in south Tibet: products of partial melting of subduction-modified lower crust. *Lithos* 96:205–224
- Guyon JH, Kapp P, Pullen A, Heizler M, Gehrels G, Ding L (2006) Tibetan basement rocks near Amdo reveal “missing” Mesozoic tectonism along the Bangong suture, central Tibet. *Geology* 34:505–508
- Hart SR (1984) A large-scale isotope anomaly in the southern Hemisphere mantle. *Nature* 309:753–757
- Hawkesworth CJ, Turner SP, McDermott F, Peate DW, Calsteren P (1997) U-Th isotopes in arc magmas: implications for element transfer from the subducted crust. *Science* 276:551–555
- He R, Zhao D, Gao R, Zheng H (2010) Tracing the Indian lithospheric mantle beneath central Tibetan plateau using teleseismic tomography. *Tectonophysics* 491:230–243
- Hellebrand E, Snow JE, Hoppe P, Hofmann AW (2002) Garnet-field melting and late-stage refertilization in ‘residual’ abyssal peridotites from the Central Indian Ridge. *J Petrol* 43:2305–2338
- Hofmann AW (1988) Chemical differentiation of the Earth: the relationship between mantle, continental crust, and oceanic crust. *Earth Planet Sci Lett* 90:297–314
- Hofmann AW (1997) Mantle geochemistry: the message from oceanic volcanism. *Nature* 385:219–229
- Holbig ES, Grove TL (2008) Mantle melting beneath the Tibetan plateau: experimental constraints on ultrapotassic magmatism. *J Geophys Res* 113:B04210. doi:10.1029/2007JB005149
- Hou ZQ, Gao YF, Qu XM, Rui ZY, Mo XX (2004) Origin of adakitic intrusives generated during mid-Miocene east-west extension in southern Tibet. *Earth Planet Sci Lett* 220:139–155
- Husson L, Conrad CP, Faccenna C (2012) Plate motions, Andean orogeny, and volcanism above the south Atlantic convection cell. *Earth Planet Sci Lett* 317–318:126–135
- Inger S, Harris N (1993) Geochemical constraints on leucogranite magmatism in the Langtang valley, Nepal Himalaya. *J Petrol* 34:345–368
- Jacobsen SB, Wasserburg GJ (1980) Sm-Nd isotopic evolution of chondrites. *Earth Planet Sci Lett* 50:139–155
- Johnson KTM (1998) Experimental determination of partition coefficients for rare earth and high-field-strength elements between clinopyroxene, garnet, and basaltic melt at high pressures. *Contrib Mineral Petrol* 133:60–68
- Johnson MC, Plank T (1999) Dehydration and melting experiments constrain the fate of subducted sediments. *Geochem Geophys Geosyst* 1:1007. doi:10.1029/1999GC000014
- Kapp P, Yin A, Manning CE, Harrison TM, Taylor MH, Ding L (2003) Tectonic evolution of the early Mesozoic blueschist-bearing Qiangtang metamorphic belt, central Tibet. *Tectonics* 22:1043. doi:10.1029/2002TC001383
- Kapp P, DeCelles PG, Gehrels GE, Heizler M, Ding L (2007) Geological records of the Lhasa-Qiangtang and Indo-Asian collisions in the Nima area of central Tibet. *Geol Soc Am Bull* 119:917–933
- Kelemen PB, Hart SR, Bernstein S (1998) Silica enrichment in the continental upper mantle via melt/rock reaction. *Earth Planet Sci Lett* 164:387–406
- Keppler H (1996) Constraints from partitioning experiments on the composition of subduction zone fluids. *Nature* 380:237–240
- Kincaid C, Griffiths RW (2004) Variability in flow and temperatures within mantle subduction zones. *Geochem Geophys Geosyst* 5:Q06002. doi:10.1029/2003GC000666
- Kincaid C, Sacks IS (1997) Thermal and dynamical evolution of the upper mantle in subduction zones. *J Geophys Res* 102(B6):12295–12315
- King J, Harris N, Argles T, Parrish R, Zhang H (2011) Contribution of crustal anatexis to the tectonic evolution of Indian crust beneath southern Tibet. *Geol Soc Am Bull* 123:218–239
- Klootwijk CT, Gee JS, Peirce JW, Smith GM, McFadden PL (1992) An early India-Asia contact: paleomagnetic constraints from Ninetyeast ridge, ODP Leg 121. *Geology* 20:395–398
- Kohn MJ, Parkinson CD (2002) Petrologic case for Eocene slab breakoff during the Indo-Asian collision. *Geology* 30:591–594
- Kosarev G, Kind R, Sobolev SV, Yuan X, Hanka W, Oreshin S (1999) Seismic evidence for a detached Indian lithospheric mantle beneath Tibet. *Science* 283:1306–1309
- Le Bas MJ, Le Maitre RW, Streckeisen A, Zanettin B (1986) A chemical classification of volcanic rocks based on the total alkali-silica diagram. *J Petrol* 27:745–750
- Le Maitre RW, Bateman P, Dudek A, Keller J, Lameyre J, Le Bas MJ, Sabine PA, Schmid R, Sorensen H, Streckeisen A, Woolley AR, Zanettin B (1989) A classification of igneous rocks and a glossary of terms. Blackwell Scientific, Oxford, pp 1–236
- Lee TY, Lawver LA (1995) Cenozoic plate reconstruction of southeast Asia. *Tectonophysics* 251:85–138
- Leech ML, Singh S, Jain AK, Klempner SL, Manickavasagam RM (2005) The onset of India-Asia continental collision: early, steep subduction required by the timing of UHP metamorphism in the western Himalaya. *Earth Planet Sci Lett* 234:83–97
- Li C, Hilst RD, Meltzer AS, Engdahl ER (2008) Subduction of the Indian lithosphere beneath the Tibetan plateau and Burma. *Earth Planet Sci Lett* 274:157–168
- Liao S, Chen Z, Luo Z, Zhou A (2002) Discovery of leucite phonolite in the Tangra Yumco area, Tibet and its geological significance. *Geol Bull China* 21:735–738 (in Chinese with English abstract)
- Liu CZ, Wu FY, Chung SL, Zhao ZD (2011) Fragments of hot and metasomatized mantle lithosphere in middle Miocene ultrapotassic lavas, southern Tibet. *Geology* 39:923–926
- Lugmair GW, Marti K (1978) Lunar initial  $^{143}\text{Nd}/^{144}\text{Nd}$ : differential evolution of the lunar crust and mantle. *Earth Planet Sci Lett* 39:349–357
- Maheo G, Guillot S, Blichert-Toft J, Rolland Y, Pêcher A (2002) A slab breakoff model for the Neogene thermal evolution of south Karakorum and south Tibet. *Earth Planet Sci Lett* 195:45–58
- McCulloch MT, Black LP (1984) Sm-Nd isotope systematics of Enderby Land granulites and evidence for the redistribution of Sm and Nd during metamorphism. *Earth Planet Sci Lett* 71:46–58

- McCulloch MT, Gamble JA (1991) Geochemical and geodynamical constraints on subduction zone magmatism. *Earth Planet Sci Lett* 102:358–374
- Melzer S, Foley SF (2000) Phase relations and fractionation sequences in potassic magma series modelled in the system  $\text{CaMgSi}_2\text{O}_6\text{-KAlSi}_3\text{O}_8\text{-Mg}_2\text{SiO}_4\text{-SiO}_2\text{-F}_2\text{O}_7$  at 1 bar to 18 kbar. *Contrib Mineral Petrol* 138:186–197
- Miller C, Schuster R, Klötzli U, Frank W, Purtscheller F (1999) Post-collisional potassic and ultrapotassic magmatism in SW Tibet: geochemical and Sr-Nd-Pb-O isotopic constraints for mantle source characteristics and petrogenesis. *J Petrol* 40:1399–1424
- Mo XX, Zhao ZD, Deng JF, Dong GC, Zhou S, Guo TY, Zhang SQ, Wang LL (2003) Response of volcanism to the India-Asia collision. *Earth Sci Front* 10:135–148 (in Chinese with English abstract)
- Mo X, Dong G, Zhao Z, Guo T, Wang L, Chen T (2005) Timing of magma mixing in the Gangdisê magmatic belt during the India-Asia collision: zircon SHRIMP U-Pb dating. *Acta Geol Sin-English Edition* 79:66–76
- Mo X, Zhao Z, Deng J, Flower M, Yu X, Luo Z, Li Y, Zhou S, Dong G, Zhu D (2006a) Petrology and geochemistry of postcollisional volcanic rocks from the Tibetan plateau: implications for lithosphere heterogeneity and collision-induced asthenospheric mantle flow. In: Dilek Y, Pavlides S (eds) *Postcollisional tectonics and magmatism in the Mediterranean Region and Asia*, vol 409. Geological Society of America, London, pp 506–530 (Special Papers)
- Mo X, Zhao Z, DePaolo D, Zhou S, Dong G (2006b) Three types of collisional and post-collisional magmatism in the Lhasa block, Tibet and implications for India intra-continental subduction and mineralization: evidence from Sr-Nd isotopes. *Acta Petrol Sin* 22:795–803 (in Chinese with English abstract)
- Mo X, Hou Z, Niu Y, Dong G, Qu X, Zhao Z, Yang Z (2007) Mantle contributions to crustal thickening during continental collision: evidence from Cenozoic igneous rocks in southern Tibet. *Lithos* 96:225–242
- Mo X, Niu Y, Dong G, Zhao Z, Hou Z, Zhou S, Ke S (2008) Contribution of syncollisional felsic magmatism to continental crust growth: a case study of the Paleogene Linzizong volcanic succession in southern Tibet. *Chem Geol* 250:49–67
- Najman Y, Appel E, Boudagher-Fadel M, Bown P, Carter A, Garzanti E, Godin L, Han J, Liebke U, Oliver G (2010) Timing of India-Asia collision: geological, biostratigraphic, and palaeomagnetic constraints. *J Geophys Res* 115:B12416. doi:10.1029/2010JB007673
- Nelson DR (1992) Isotopic characteristics of potassic rocks: evidence for the involvement of subducted sediments in magma genesis. *Lithos* 28:403–420
- Nelson KD, Zhao W, Brown LD, Kuo J, Che J, Liu X, Klemperer SL, Makovsky Y, Meissner R, Mechie J, Kind R, Wenzel F, Ni J, Nabelek J, Leshou C, Tan H, Wei W, Jones AG, Booker J, Unsworth M, Kidd WSF, Hauck M, Alsdorf D, Ross A, Cogan M, Wu C, Sandvol E, Edwards M (1996) Partially molten middle crust beneath southern Tibet: synthesis of project INDEPTH results. *Science* 274:1684–1688
- Nixon P, Thirlwall M, Buckley F, Davies C (1984) Spanish and Western Australian lamproites: aspects of whole rock geochemistry. In: Kornprobst J (ed) *Kimberlites I. Kimberlites and related rocks*. Elsevier, Amsterdam, pp 285–296
- Nomade S, Renne PR, Mo X, Zhao Z, Zhou S (2004) Miocene volcanism in the Lhasa block, Tibet: spatial trends and geodynamic implications. *Earth Planet Sci Lett* 221:227–243
- Owen JP (2008) Geochemistry of lamprophyres from the Western Alps, Italy: implications for the origin of an enriched isotopic component in the Italian mantle. *Contrib Mineral Petrol* 155:341–362
- Pan G, Ding J, Yao D, Wang L (2004) An introduction of geological map of the Tibetan Plateau and neighbouring area. Chengdu Map Press, Chengdu, pp 1–133 (in Chinese)
- Patriat P, Achache J (1984) India-Eurasia collision chronology has implications for crustal shortening and driving mechanism of plates. *Nature* 311:615–621
- Pearce J (1982) Trace element characteristics of lavas from destructive plate boundaries. In: Thorpe RS (ed) *Andesites: orogenic andesites and related rocks*. John Wiley, New York, pp 525–548
- Pearce JA, Mei H (1988) Volcanic rocks of the 1985 Tibet geotraverse: Lhasa to Golmud. *Phil Trans R Soc Lond A* 327:169–201
- Pearce JA, Parkinson IJ (1993) Trace element models for mantle melting: application to volcanic arc petrogenesis. In: Prichard HM, Alabaster T, Harris NBW, Neary CR (eds) *Magmatic processes and plate tectonics*. Geol Soc London Spec Pub 76:373–403
- Perini G, Francalanci L, Davidson JP, Conticelli S (2004) Evolution and genesis of magmas from Vico volcano, central Italy: multiple differentiation pathways and variable parental magmas. *J Petrol* 45:139–182
- Pfänder JA, Münker C, Stracke A, Mezger K (2007) Nb/Ta and Zr/Hf in ocean island basalts—implications for crust-mantle differentiation and the fate of Niobium. *Earth Planet Sci Lett* 254:158–172
- Plank T, Langmuir CH (1998) The chemical composition of subducting sediment and its consequences for the crust and mantle. *Chem Geol* 145:325–394
- Prelević D, Foley SF, Romer R, Conticelli S (2008) Mediterranean Tertiary lamproites derived from multiple source components in postcollisional geodynamics. *Geochim Cosmochim Acta* 72:2125–2156
- Qu X, Hou Z, Li Y (2004) Melt components derived from a subducted slab in late orogenic ore-bearing porphyries in the Gangdese copper belt, southern Tibetan plateau. *Lithos* 74:131–148
- Qu XM, Hou ZQ, Zaw K, Mo XX, Xu WY, Xin HB (2009) A large-scale copper ore-forming event accompanying rapid uplift of the southern Tibetan Plateau: evidence from zircon SHRIMP U-Pb dating and LA ICP-MS analysis. *Ore Geol Rev* 36:52–64
- Replumaz A, Karason H, Van der Hilst RD, Besse J, Taponnier P (2004) 4-D evolution of SE Asia's mantle from geological reconstructions and seismic tomography. *Earth Planet Sci Lett* 221:103–115
- Richards A, Argles T, Harris N, Parrish R, Ahmad T, Darbyshire F, Draganits E (2005) Himalayan architecture constrained by isotopic tracers from clastic sediments. *Earth Planet Sci Lett* 236:773–796
- Rickwood PC (1989) Boundary lines within petrologic diagrams which use oxides of major and minor elements. *Lithos* 22:247–263
- Rogers N, Hawkesworth C, Parker R, Marsh J (1985) The geochemistry of potassic lavas from Vulcini, central Italy and implications for mantle enrichment processes beneath the Roman region. *Contrib Mineral Petrol* 90:244–257
- Royden LH, Burchfiel BC, Van der Hilst RD (2008) The geological evolution of the Tibetan plateau. *Science* 321:1054–1058
- Scharer U (1984) The effect of initial  $^{230}\text{Th}$  disequilibrium on young U-Pb ages: the Makalu case, Himalaya. *Earth Planet Sci Lett* 67:191–204
- Steiger RH, Jäger E (1977) Subcommittee on geochronology: convention of the use of decay constants in geo- and cosmochronology. *Earth Planet Sci Lett* 36:259–362
- Sun S-S, McDonough WF (1989) Chemical and isotopic systematics of ocean basalts: implications for mantle composition and processes. In: Saunders AD, Norry MJ (eds) *Magmatism in the ocean basins*. Geol Soc Spec Publ 42:313–345
- Sun CG, Zhao ZD, Mo XX, Zhu DC, Dong GC, Zhou S, Chen HH, Xie LW, Yang YH, Sun JF, Yu F (2008) Enriched mantle source

- and petrogenesis of Sailipu ultrapotassic rocks in southwestern Tibetan plateau: constrains from zircon U-Pb geochronology and Hf isotopic compositions. *Acta Petrol Sin* 24:249–264 (in Chinese with English abstract)
- Sun Z, Pei J, Li H, Xu W, Jiang W, Zhu Z, Wang X, Yang Z (2012) Palaeomagnetism of late Cretaceous sediments from southern Tibet: evidence for the consistent palaeolatitudes of the southern margin of Eurasia prior to the collision with India. *Gondwana Res* 21:53–63
- Tapponnier P, Xu Z, Roger F, Meyer B, Arnaud N, Wittlinger G, Yang J (2001) Oblique stepwise rise and growth of the Tibet plateau. *Science* 294:1671–1677
- Tatsumi Y, Hamilton D, Nesbitt RW (1986) Chemical characteristics of fluid phase released from a subducted lithosphere and origin of arc magmas: evidence from high-pressure experiments and natural rocks. *J Volcanol Geotherm Res* 29:293–309
- Tilmann F, Ni J, Team IIS (2003) Seismic imaging of the downwelling Indian lithosphere beneath central Tibet. *Science* 300:1424–1427
- Turner S, Hawkesworth C, Liu J, Rogers N, Kelley S, Van Calsteren P (1993) Timing of Tibetan uplift constrained by analysis of volcanic rocks. *Nature* 364:50–54
- Turner S, Arnaud N, Liu J, Rogers N, Hawkesworth C, Harris N, Kelley S, Van Calsteren P, Deng W (1996) Post-collision, shoshonitic volcanism on the Tibetan plateau: implications for convective thinning of the lithosphere and the source of ocean island basalts. *J Petrol* 37:45–71
- Turner S, Hawkesworth C, Rogers N, Bartlett J, Worthington T, Hergt J, Pearce J, Smith I (1997) 238U–230Th disequilibria, magma petrogenesis, and flux rates beneath the depleted Tonga-Kermadec island arc. *Geochim Cosmochim Acta* 61:4855–4884
- Turner S, Bourdon B, Gill J (2003) Insights into magma genesis at convergent margins from U-series isotopes. *Rev Mineral Geochim* 52:255–315
- Venturelli G, Capedri S, Battistini GD, Crawford A, Kogarko LN, Celestini S (1984) The ultrapotassic rocks from southeastern Spain. *Lithos* 17:37–54
- Wang Y, Deng T, Biasatti D (2006) Ancient diets indicate significant uplift of southern Tibet after ca. 7 Ma. *Geology* 34:309–312
- Wen DR, Chung SL, Song B, Iizuka Y, Yang HJ, Ji J, Liu D, Gallet S (2008) Late Cretaceous Gangdese intrusions of adakitic geochemical characteristics, SE Tibet: petrogenesis and tectonic implications. *Lithos* 105:1–11
- Williams H, Turner S, Kelley S, Harris N (2001) Age and composition of dikes in southern Tibet: new constraints on the timing of east-west extension and its relationship to postcollisional volcanism. *Geology* 29:339–342
- Williams HM, Turner SP, Pearce JA, Kelley SP, Harris NBW (2004) Nature of the source regions for post-collisional, potassic magmatism in southern and northern Tibet from geochemical variations and inverse trace element modelling. *J Petrol* 45:555–607
- Wilson M (1989) *Igneous petrogenesis: a global tectonic approach*. Unwin Hyman, London
- Woodhead JD, Hergt JM, Davidson JP, Eggins SM (2001) Hafnium isotope evidence for ‘conservative’ element mobility during subduction zone processes. *Earth Planet Sci Lett* 192:331–346
- Workman RK, Hart SR (2005) Major and trace element composition of the depleted MORB mantle (DMM). *Earth Planet Sci Lett* 231:53–72
- Xie G, Zou A, Yuan J, Li X, Liao S, Tang F, Huang C, Chen Z, Xu Z (2004) New results and major progress in regional geological survey of the Boindoi district and Comai sheets. *Geol Bull China* 23:498–505 (in Chinese with English abstract)
- Xu YG, Lan JB, Yang QJ, Huang XL, Qiu HN (2008) Eocene break-off of the Neo-Tethyan slab as inferred from intraplate-type mafic dykes in the Gaoligong orogenic belt, eastern Tibet. *Chem Geol* 255:439–453
- Yi Z, Huang B, Chen J, Chen L, Wang H (2011) Paleomagnetism of early Paleogene marine sediments in southern Tibet, China: implications to onset of the India-Asia collision and size of Greater India. *Earth Planet Sci Lett* 309:153–165
- Yin A, Harrison TM (2000) Geologic evolution of the Himalayan-Tibetan orogen. *Annu Rev Earth Planet Sci* 28:211–280
- Yin A, Harrison TM, Ryerson FJ, Chen W, Kidd W, Copeland P (1994) Tertiary structural evolution of the Gangdese thrust system, southeastern Tibet. *J Geophys Res* 99:18175–18201
- Zhang JH, Gao S, Ge WC, Wu FY, Yang JH, Wilde SA, Li M (2010) Geochronology of the Mesozoic volcanic rocks in the Great Xing’an Range, northeastern China: implications for subduction-induced delamination. *Chem Geol* 276:144–165
- Zhang FQ, Chen HL, Yu X, Dong CW, Yang SF, Pang YM, Batt GE (2011) Early Cretaceous volcanism in the northern Songliao basin, NE China, and its geodynamic implication. *Gondwana Res* 19:163–176
- Zhao ZD, Mo XX, Nomade S, Renne PR, Zhou S, Dong GC, Wang LL, Zhu DC, Liao ZL (2006) Post-collisional ultrapotassic rocks in Lhasa block, Tibetan plateau: spatial and temporal distribution and its implications. *Acta Petrol Sin* 22:787–794 (in Chinese with English abstract)
- Zhao ZD, Mo XX, Sun CG, Niu YL, Dong GC, Zhou S, Dong X, Liu YS (2008) Mantle xenoliths in southern Tibet: geochemistry and constraints for the nature of the mantle. *Acta Petrol Sin* 24:193–202 (in Chinese with English abstract)
- Zhao Z, Mo X, Dilek Y, Niu Y, DePaolo DJ, Robinson P, Zhu D, Sun C, Dong G, Zhou S, Luo Z, Hou Z (2009) Geochemical and Sr-Nd-Pb-O isotopic compositions of the post-collisional ultrapotassic magmatism in SW Tibet: petrogenesis and implications for India intra-continental subduction beneath southern Tibet. *Lithos* 113:190–212
- Zhao JM, Yuan XH, Liu HB, Kumar P, Pei SP, Kind R, Zhang ZJ, Teng JW, Ding L, Gao X, Xu Q, Wang W (2010) The boundary between the Indian and Asian tectonic plates below Tibet. *Proc Natl Acad Sci USA* 107:11229–11233
- Zhao WJ, Kumar P, Mechie J, Kind R, Meissner R, Wu ZH, Shi DN, Su HP, Xue GQ, Karplus M, Tilmann F (2011) Tibetan plate overriding the Asian plate in central and northern Tibet. *Nat Geosci* 4:870–873
- Zhou H, Murphy MA (2005) Tomographic evidence for wholesale underthrusting of India beneath the entire Tibetan plateau. *J Asian Earth Sci* 25:445–457
- Zhou S, Mo X, Dong G, Zhao Z, Qiu R, Guo T, Wang L (2004)  $^{40}\text{Ar}$ - $^{39}\text{Ar}$  geochronology of Cenozoic Linzizong volcanic rocks from Linzhou basin, Tibet, China, and their geological implications. *Chin Sci Bull* 49:1970–1979
- Zhu B, Kidd WSF, Rowley DB, Currie BS, Shafique N (2005) Age of initiation of the India-Asia collision in the east-central Himalaya. *J Geol* 113:265–285
- Zhu DC, Pan GT, Chung SL, Liao ZL, Wang LQ, Li GM (2008) SHRIMP zircon age and geochemical constraints on the origin of lower Jurassic volcanic rocks from the Yeba Formation, southern Gangdese, south Tibet. *Int Geol Rev* 50:442–471
- Zindler A, Hart S (1986) Chemical geodynamics. *Ann Rev Earth Planet Sci* 14:493–571